Journal of Phycology
October 2023, Volume 59 Issue 5 Pages 1064-1084
https://doi.org/10.1111/jpy.13382
https://archimer.ifremer.fr/doc/00851/96259/

Does dinocyst wall composition really reflect trophic affinity? New evidence from ATR micro- FTIR spectroscopy measurements

Meyvisch Pjotr [1,*], Mertens Kenneth [2], Gurdebeke Pieter Roger [1], Sandt Christophe [3], Pospelova Vera [4], Vrielinck Henk [5], Borondics Ferenc [3], Louwye Stephen [1]

[1] Department of Geology Ghent University Ghent, Belgium
[2] Ifremer, LITTORAL ,France
[3] SMIS Beamline, SOLEIL Synchrotron Paris ,France
[4] Department of Earth and Environmental Sciences University of Minnesota Minneapolis Minnesota, USA
[5] Department of Solid-State Sciences Ghent University Ghent, Belgium

* Corresponding author : Pjotr Meyvisch, email address : pjotr.meyvisch@ugent.be

Abstract :

Attenuated total reflection (ATR) microscope Fourier transform infrared (micro-FTIR) spectroscopy was used to investigate the dinosporin composition in the walls of modern, organic-walled dinoflagellate resting cysts (dinocysts). Variable cyst wall compositions were observed, which led to the erection of four spectrochemical groups, some with striking similarities to other resistant biomacromolecules such as sporopollenin and algaenan. Furthermore, possible proxies derivable from the spectrochemical composition of modern and fossil dinocysts were discussed. The color of the dinocyst walls was reflected in the spectral data. When comparing that color with a standard and the results of a series of bleaching experiments with oxidative agents, eumelanin was assigned as a likely pigment contributing to the observed color. Following this assignment, the role of eumelanin as an ultraviolet sunscreen in colored dinocysts was hypothesized, and its implications on the autofluorescence and morphological preservation of dinocysts were further discussed. Unlike what had previously been assumed, it was shown that micro-FTIR data from dinocysts cannot be used to unambiguously infer trophic affinities of their associated cells. Finally, using methods with high spatial resolutions (synchrotron transmission micro-FTIR and optical photothermal infrared spectroscopy), it was shown that dinocyst wall layers are chemically homogenous at the probed scales. This study fills a large knowledge gap in our understanding of the chemical nature of dinocyst walls and has nuanced certain assumptions and interpretations made in the past.

Keywords : attenuated total reflection micro-Fourier transform infrared spectroscopy, bleaching, dinosporin composition, optical photothermal infrared spectroscopy, organic-walled dinocysts, pigments, spectrochemical methods, sunscreen, synchrotron radiation, trophic affinity

Abbreviations

ATR, attenuated total reflection; BA, barrier filter; BP, bandpass filter; CLB, cellulose-like backbone; DM, dichroic mirror; FTIR, Fourier transform infrared; HAB, harmful algal bloom; HCl, hydrochloric acid; HF, hydrofluoric acid; IR, infrared; MAAs, mycosporine-like amino acids; MCT, mercury cadmium telluride; NA, numerical aperture; O-PTIR, optical photothermal infrared; PBC, polynomial baseline correction; PKSs, polyketide synthases; QCL, quantum cascade laser; SG, Savitzky-Golay; SNR, signal-to-noise ratio; SPT, sodium polytungstate; UV, ultraviolet

1. INTRODUCTION

Dinoflagellates are a biologically diverse group of aquatic microorganisms with mainly planktonic, but also benthic, symbiotic, and parasitic forms, including species which can produce toxins and cause harmful algal blooms (HABs) (e.g., Hackett et al., 2004; Lundholm et al., 2022; Smayda, 2002; Taylor, 1987; Taylor et al., 2008). Dinoflagellates exhibit a variety of feeding strategies ranging from exclusive autotrophy to exclusive heterotrophy, with intermediate obligatory or facultative mixotrophy (e.g., Schnepf and Elbrächter, 1992; Stoecker, 1999). Their prey types can be diverse, ranging from single bacterial cells to other protists and even other dinoflagellates (e.g., Jacobson and Anderson, 1986; Jeong et al., 2010). The determination of dinoflagellate trophic affinities is important since abundances and ratios of heterotrophic vs. autotrophic species are commonly used as indicators for natural and human-induced eutrophication (e.g., Li et al., 2020; Penaud et al., 2018), ecology (Rodrigues, 2022), and as paleoclimatological and paleoenvironmental proxies (e.g., Penaud et al., 2018; Pospelova et al., 2006). Deriving the trophic affinity is not always

[1]Date of submission: 31/07/2023

straightforward and over the last few decades, many autotrophic dinoflagellates were found to be mixotrophic, among which many species responsible for HABs (García-Oliva et al., 2022). Approximately 90% of known extant species live in marine to brackish environments, with the remainder restricted to freshwater settings (Taylor et al., 2008). Marine taxa generally occur within temperature-defined broad latitudinal and neritic zones (Taylor, 1987). Predominantly motile, autotrophic freshwater taxa generally show a high endemism, seasonality, and stronger eutrophication responses, and occur in ponds and lakes at vastly different altitudes (Pollingher, 1987). Approximately 13–16% (~200) of extant dinoflagellate species produce dormant resting cysts (dinocysts or hypnozygotes, from here on referred to as 'cysts', unless otherwise specified) often during a diploid stage in their otherwise haplophasic lifecycle (Head, 1996). Besides the occurrence of calcareous and silicious forms, most cysts are organic-walled, sometimes with multiple wall layers (Evitt, 1985). These are highly resistant to physical and chemical degradation, explaining the occurrence of more than 2500 described fossil morphospecies, the oldest dating as far back as the Triassic (240 million years ago; e.g., Mangerud et al., 2019; Taylor et al., 2008). The main known functions of cysts include nuclear replenishment and recombination through meiosis, aiding in propagation and dispersion, as well as providing protection against unfavorable conditions, predation, and parasitic attack (Bravo & Figueroa, 2014). Walls of modern cysts are often transparent, though their color can range from light yellow to dark brown and can be an important taxonomic trait (Matsuoka & Fukuyo, 2000). Colored cysts are known to be less resistant to oxidizing agents and acetolysis (Brenner, 1998; Dale, 1976; Marret, 1993; Persson & Smith, 2022; Reid, 1977) and less autofluorescent (Brenner and Biebow, 2001) than transparent forms. Most of the modern, exclusively heterotrophic, cyst-forming dinoflagellates form colored cysts, while most autototrophic and mixotrophic species produce transparent cysts,

though exceptions exist (e.g., *Gymnodinium catenatum*, *Parvodinium umbonatum, Polykrikos hartmanii*, *Trinovantedinium applanatum*).

Surprisingly little is known about the composition of cyst walls and the factors contributing to its variability. They have long been thought to consist of a suite of refractory biomacromolecules known as dinosporin (Fensome et al., 1993), which is believed to be compositionally different from other resistant biomacromolecules such as algaenan and sporopollenin found in the walls of mostly freshwater green algae and spores and pollen, respectively (e.g., Kokinos et al., 1998). A highly detailed characterization of the molecular building blocks of dinosporin requires the use of costly and time-consuming analytical methods like temperature-resolved, Curie-point pyrolysis-gas chromatography and flash pyrolysis-gas chromatography-mass spectrometry for which often very clean cysts (de Leeuw et al., 2006) and large sample volumes are needed (several 100–1000 cysts). Therefore, such studies are rare and have yielded notably different results in the past; for modern cysts, Kokinos et al. (1998) used cultured *Lingulodinium machaerophorum* and reported a relatively condensed and strongly aromatic macromolecular buildup, devoid of carotenoids and with tocopherol as a major building block. Contrastingly, for the same species, Versteegh et al. (2012) suggested a strongly cross-linked carbohydrate-based polymer devoid of tocopherol and hypothesized that the differential outcome might be due to dissimilarities in the cyst wall isolation and purification methods used and/or unwanted contaminants.

An alternative, relatively low-cost, and rapid method for investigating cyst wall compositions is Fourier transform infrared (FTIR) spectroscopy, which provides a broader macromolecular picture by detecting molecular vibrations induced by probing the sample with infrared (IR) radiation at specific frequencies (expressed in wavenumbers, usually mid-

IR = 4000–400 cm^{-1}). The resulting data yield spectra with absorption bands whose positions correlate to constituent atom types, their mutual covalent bond types, and their local functional group. By using a microscope (micro-FTIR), the IR beam can be carefully aligned and focused to a spot size close to the mid-infrared diffraction limit of ~10 µm. Hence, spectra from individual cysts (usually 20–60 µm in size) can be retrieved, allowing inter and intraspecific spectrochemical comparisons. A method based on attenuated total reflection (ATR) micro-FTIR spectroscopy was evaluated to be most optimal for such comparisons (Meyvisch et al., 2022). The main advantages FTIR spectroscopy over the mass spectrometry-based methods mentioned earlier are: (i) smaller required sample volumes, (ii) better cost vs. time efficiency (allowing relatively rapid upscaling diverse datasets), and (iii) the yield of macromolecular information. The main disadvantage is that it provides a less detailed and semi-quantitative molecular picture. ATR micro-FTIR spectra from dinocysts are currently not fully quantitative, as this requires calibration models using the concentrations of the main macromolecules present in the cysts. Further common processing and interpretation options for these spectra were described by Meyvisch et al. (2022).

Micro-FTIR has previously been applied to assess compositional differences between fossil *Thalassiphora pelagica* cysts from oxic and sulphidic depositional environments (Versteegh et al., 2007, 2020), as a chemotaxonomical tool for distinguishing between morphologically similar fossil (*Apectodinium* complex; Bogus et al., 2012) and modern cysts (Gurdebeke et al., 2018, 2020, 2021), for studying organic-walled division cysts of *Unruhdinium penardii* var. *robustum* (Mertens et al. 2021) and as a tool for inferring trophic affinities of associated, modern, motile dinoflagellate cells (Bogus et al., 2014; Gurdebeke, 2019). Most of the abovementioned studies used a non-optimal data collection method (i.e.,

149 transflection micro-FTIR spectroscopy; Meyvisch et al. 2022) and relatively small datasets
150 (<30 spectra) containing a limited number of taxa (usually <10).
151
152 The main objectives of this study were (i) to further explore the chemical variability of
153 dinosporin, and (ii) to reassess the relation between dinocyst wall composition and its color,
154 as well as its inferred trophic affinity. This was done via the collection of a large dataset of
155 211 ATR micro-FTIR spectra from a wide range of modern, colored and transparent, auto-,
156 mixo- and heterotrophic dinocyst taxa, isolated from a collection of surface sediment samples
157 from the Northern Hemisphere. To specifically test the correlation between cyst wall
158 composition and trophic affinity, exceptional cyst taxa such as the transparent heterotroph
159 *Trinovantedinium applanatum* and the dark brown-colored autotroph *Parvodinium*
160 *umbonatum* were also included in this dataset. In some additional experiments, several cysts
161 were exposed to oxidizing agents such as ultraviolet-A (UV-A) radiation (315–400 nm) and
162 hydrogen peroxide (H_2O_2) and their bleaching behavior was monitored. This task was carried
163 out to assess the effects of loss of color on their chemical composition, and whether any
164 visible morphological changes occur during oxidation. Finally, the compositional variability
165 within 169 single cyst specimens was investigated by using spectrochemical methods with a
166 high spatial resolution, i.e., synchrotron radiation transmission micro-FTIR spectroscopy (~6
167 × 6 μm^2 spot size) and optical photothermal infrared (O-PTIR) spectroscopy (~0.5 × 0.5
168 μm^2 spot size).
169
170 ## 2. MATERIALS AND METHODS
171
172 ### *2.1 Sample selection, processing and dinocyst isolation*
173

Modern surface sediment samples from diverse marine, brackish and freshwater environments in the Northern Hemisphere were used in this study; some of which were processed using room temperature 7.3% hydrochloric acid (HCl) and warm (60 °C) 40% hydrofluoric acid (HF) (Table S1). In addition, a specimen from a macerated drill core sample from the Cretaceous of Belgium (Coniacian–Santonian) was studied (Table S1). The common goal of all used processing steps was to yield residues containing clean and readily extractable cysts, while minimizing chances for inducing chemical alteration of the samples in the process. Besides occasional acid treatment, other common methods included ultrasonication, sodium polytungstate (SPT; 2.1 $g \cdot cm^{-3}$) heavy liquid density separation, filtering (125 and 8 µm) and decanting. From the processed residues, individual cysts were identified, photographed, isolated, and deposited on measurement substrates (IR-grade 2.54 cm diameter CaF_2-disk for Synchrotron transmission micro-FTIR and O-PTIR spectroscopy; 5 × 5 cm IR-enhanced Au mirror for ATR micro-FTIR spectroscopy) via a protocol described in Meyvisch et al. (2022). Several solid aggregates of a *Sepia officinalis* eumelanin (Sigma M2649) and crystals of a microcrystalline cellulose (Sigma 435236) standard were also analyzed (Sigma-Aldrich, St. Louis, Missouri, USA).

2.2 ATR micro-FTIR spectroscopy

2.2.1 Data collection

ATR micro-FTIR spectra of individual cysts and standards were recorded at Ghent University using a Bruker Vertex 80v spectrometer (Bruker, Billerica, USA) with Globar IR source coupled to a Hyperion 2000 infrared (IR) microscope. Using a liquid N_2-cooled mercury cadmium telluride (MCT) detector in the microscope and a KBr beam splitter in the

199 bench spectrometer, IR spectral ranges of 4500–600 cm^{-1} were recorded in atmospheric
200 conditions at 4 cm^{-1} resolution with 256 scans. The germanium ATR crystal ($\eta = 4.0$; 100
201 µm tip diameter) was mounted on the 20 × (0.6 NA) objective of the Hyperion microscope. A
202 new background spectrum was recorded every 3–5 measurements. Practicalities concerning
203 background and sample measurements and cleaning of the ATR crystal between
204 measurements can be found in Meyvisch et al. (2022).
205
206 *2.2.2 Data processing*
207
208 Using OPUS 8.2.21 (Bruker) software, atmospheric contributions from CO_2 and H_2O
209 were subtracted from all ATR spectra which were subsequently exported as individual *.txt
210 files and merged into a dataframe (*.xlsx) with added metadata using RStudio (Team RS,
211 2020) (Table S2). The resulting dataset was further processed in Quasar 1.7.0 (Demsar et al.,
212 2013; Toplak et al., 2021). Spectral processing was carried out in Quasar's "Preprocess
213 Spectra" widget from the "Spectroscopy" add-on (version 0.6.9) and was done in two ways,
214 depending on further usage of the data: (i) For visual spectral comparisons, processing
215 included (in that order): Savitzky-Golay (SG) filtering (window size = 11, polynomial order
216 = 2, derivative order = 0), polynomial baseline correction (PBC; rubberband method), cutting
217 out regions of either 4000–600 cm^{-1} or 1800–600 cm^{-1}, vector normalization, and
218 averaging. For calculating second derivatives (to detect peak positions, especially of partially
219 overlapping bands), the derivative order during SG filtering was set to 2 (other parameters
220 were kept the same) and the PBC was left out; (ii) For principal component analysis (PCA),
221 processing included (in that order): cutting out regions of both 3000–2800 cm^{-1} and 1800–
222 600 cm^{-1}, PBC, Savitzky-Golay (SG) filtering (window size = 11, polynomial order = 2,
223 derivative order = 0), and vector normalization. Here it was opted to cut out the spectral

224 regions of interest prior to PBC and normalization in order to prevent interferences of noise
225 and deviations in the baselines from spectrally uninformative regions during subsequent
226 processing steps. These processed spectra were then fed into Quasar's "PCA" (principal
227 component analysis) widget with the parameter box "Normalize variables" unchecked. The
228 first two components (PC1 and PC2) were kept, as they explained most the variance in the
229 dataset (see results).
230
231 *2.3 Dinocyst bleaching*
232
233 Bleaching experiments were carried out at Ifremer LER BO (Concarneau, France).
234 Two types of bleaching (i.e., oxidizing) agents were used: H_2O_2 and UV-A light. For H_2O_2
235 bleaching, individual cysts were isolated from filtered and density separated (SPT, 1.4 $g \cdot$
236 cm^{-3}) surface sediment residues (Table S3) and were deposited in polystyrene Falcon®
237 Multiwells™ (Corning, New York, USA) containing 0.5 ml Millipore Milli-Q® water (Merck
238 Millipore, Burlington, Massachusetts, USA). The isolated specimens were first photographed
239 at 400 × magnification under an IX70 microscope (Olympus, Tokyo, Japan). Afterwards 0.5
240 ml of 30% H_2O_2 was added and several s later, images at 1 $frame \cdot s^{-1}$ were recorded for
241 usually several mins onwards. For UV-A bleaching individual specimens were isolated from
242 the same processed residues, deposited on a glass slide with a cover slip and photographed at
243 1000 × magnification, using a BX41 fluorescence microscope (Olympus, Tokyo, Japan).
244 Afterwards, specimens were illuminated with the microscope's built-in UV-A source (U-
245 MWU2 epifluorescence filter sets; excitation: BP330–385; beam splitter: DM400; emission:
246 BA420), while recording images at 1 $frame \cdot s^{-1}$. Bleached cysts were extracted from the
247 wells and slides and transferred to drops of distilled water. Leftover cell contents were
248 removed by piercing and manipulating the cysts with a sterile 0.02 mm stainless steel

dissection needle (Fine Science Tools Inc., Foster City, California, USA) and by transferring them to clean drops of distilled water. After cleaning, specimens were transferred to an Au mirror for ATR micro-FTIR analysis at Ghent University.

2.4 Synchrotron transmission micro-FTIR spectroscopy

These analyses were done in June 2021 at the SMIS beamline (synchrotron SOLEIL, France). Spectra were collected in transmission mode using a Thermo Nicolet 8700 spectrometer (Thermo Fisher Scientific Inc., Waltham, Massachusetts, USA) coupled to a TFS Continuum microscope equipped with a liquid N_2-cooled $50 \times 50\ \mu m^2$ MCT detector, using a $32 \times$ (0.65 NA) Schwarzschild objective and matching condenser. The microscope aperture was set to $6 \times 6\ \mu m^2$. Prior to each measurement, the microscope was focused on the middle of the dinocyst specimen, the condenser was manually aligned to maximize detected IR signal intensities, and a background spectrum was recorded on an empty region of the CaF_2 disk several tens of µm away from the sample. Hyperspectral maps of individual dinocyst specimens were measured by raster scanning the sample in 3 or 4 µm steps. IR spectral ranges of 4000–850 cm^{-1} were recorded in atmospheric conditions at cm^{-1} resolution with 80 scans. For initial data visualization, the software Omnic 9.2 (Thermo Fisher Scientific Inc., Waltham, Massachusetts, USA) was used. Further spectral processing was also done in Quasar 1.7.0 (comparable to the ATR data; see subsection 2.2.2) and included (in that order): SG filtering (window size = 15, polynomial order = 2, derivative order = 0), cutting out region of 1800–900 cm^{-1}, PBC, vector normalization and averaging. Figures were exported in *.svg format and further processed in Inkscape 1.2.2 (Inkscape Project, 2020).

274 *2.5 O-PTIR spectroscopy*

275

276 O-PTIR analyses were done with a mIRage IR microscope (Photothermal
277 Spectroscopy Corp., Santa Barbara, USA) from the SMIS extension lab (synchrotron
278 SOLEIL, France). Spectra were collected in reflection mode at 2 cm^{-1} spectral resolution in
279 "High signal-to-noise ratio (SNR) mode" (100 $cm^{-1} \cdot s^{-1}$ sweep speed), through a 40 × (0.78
280 NA), 8 mm working distance Schwarzschild objective (spot size ~0.5 µm). The IR source
281 was a pulsed, tunable four-stage quantum cascade laser (QCL) scanning in the following
282 wavenumber ranges: 3026–2700, 1800–1510, 1510–1200 and 1200–920 cm^{-1}. The reflected
283 IR light was detected with a high-sensitivity avalanche photodiode. The probe was a
284 continuous wave 532 nm visible laser with variable power. The power of the QCL was set to
285 either 46, 78 or 100% (~1.5–3 mW on the sample) and that of the probe laser to either 0.25 or
286 0.50% (~80–150 µW on the sample) to optimize detected signal intensities while prohibiting
287 oversaturation and, in case of the probe laser, photodamage to the sample. For some
288 dinocysts, single spectra (29 s per spectrum) were collected from different locations on the
289 specimens, after iteratively adjusting the laser focal depth for optimizing detected signal
290 intensities. For other specimens line scans and arrays (i.e., hyperspectral maps) were collected
291 with varying line and grid spacings, depending on the size of the dinocyst or feature of
292 interest. All hyperspectral maps were measured by averaging two spectra at each point in the
293 line or grid. For initial data visualization PTIR-studio (Photothermal Spectroscopy Corp.) was
294 used. Further spectral processing was also done in Quasar 1.7.0 (comparable to the ATR data;
295 see subsection 2.2.2) and included (in that order): cutting out region of 1800–950 cm^{-1}, PBC,
296 SG filtering (window size = 11, polynomial order = 2, derivative order = 0), vector
297 normalization and averaging.

298

299 # 3. RESULTS

300

301 ## *3.1 ATR micro-FTIR spectroscopy*

302

303 A total of 211 empty and clean, modern cysts (10 families, 24 genera, 50 species) from
304 17 different locations were analyzed via ATR micro-FTIR spectroscopy (dataset in Table S2,
305 additional metadata in Table S3). At least two reproducible spectra were recorded for each
306 taxon or defined complex. The raw spectra all showed a comparable, nonlinear, sloping
307 baseline (due to the reflection of the evanescent wave on the Au measurement substrate)
308 which was subtracted using a PBC. The regions of 4000–600 cm^{-1} and 1800–600 cm^{-1} were
309 used for visual spectral comparisons (Figure 1a–b) and constituting absorption bands were
310 identified using the literature (Table 1). Most of the recorded spectral variation between taxa
311 was found in a part of the high wavenumber and fingerprint regions (3000–2800 cm^{-1}, 1800–
312 600 cm^{-1} respectively; Figure 1b), therefore these regions were the focus for further PCA
313 (Figure 1a–d, Figure 2). The spectral variation in these regions was reflected in the amount of
314 variance explained by the first two components (PC1: 73.5%, PC2: 12.8%, together: 86.3%).

315

316 ## *3.2 Dinocyst bleaching and subsequent ATR micro-FTIR spectroscopy*

317

318 A total of 33 isolated, modern cyst specimens were bleached (17 H_2O_2, 16 UV-A). Of
319 those, 18 (15 H_2O_2, three UV-A) were analyzed via ATR micro-FTIR spectroscopy, of which
320 six (one H_2O_2, five UV-A) specimens are presented here (Figure 3, Figures S1–S2, Videos
321 S1–S4; data in Table S2, additional metadata in Table S3). For both methods, visible
322 bleaching and movement of the cyst wall and the cellular contents started within a few s after
323 introducing the oxidative agents (Videos S1–S4). Bleaching speeds were higher for the used

UV-A source than the used volume and concentration of H_2O_2. The red body in taxa with colored cyst walls lost most of its color after approx. 5.50 mins of UV-A exposure (Video S1), while this was generally shorter, approx. 3.50 mins, for taxa with transparent cyst walls and (Video S2). Taxa with colored cyst walls and processes and/or ridges progressively reduced or lost their color and ornamentation during UV and chemical bleaching, while this was not the case for taxa with transparent cyst walls and often equally delicate ornamentation (Figures S1–S2, Videos S2–S3).

3.3 Synchrotron transmission micro-FTIR spectroscopy

A total of 169 cyst specimens (123 modern, 46 fossil) were analyzed via synchrotron transmission micro-FTIR spectroscopy. Five specimens (three modern, two fossil) were fully mapped, for three modern specimens line scans (e.g., from process to central body) were recorded and for 13 specimens (six modern, seven fossil discrete point measurements from the central body and ornamentation were obtained. Single spectra were extracted from the 148 remaining specimens. One mapped specimen from the Coniacian–Santonian of Belgium is presented (Figure 4a, dataset in Table S4). All transmission spectra showed expected scattering and interference artifacts, mainly visible in the region of 4000–1800 cm^{-1} (not shown here). The region of 1800–900 cm^{-1} was selected for visual spectral comparisons (Figure 4b).

3.4 O-PTIR spectroscopy

A total of 93 cyst specimens (69 modern, 24 fossil) were analyzed via O-PTIR spectroscopy. Sixteen specimens (10 modern, six fossil) were fully mapped with step sizes

varying from 1–5 µm, for another 16 specimens (11 modern, five fossil) line scans were recorded and for the remaining 61 specimens at least three discrete point measurements from different regions of the cysts were taken. Four modern specimens are presented (Figure 4c, dataset in Table S5, analyzed areas in Figure S3). The region of 1800–950 cm^{-1} was selected for visual spectral comparisons, as the data from 950–920 cm^{-1} was generally noisy. Colored cysts were more susceptible to getting photodamaged by the laser than transparent cysts. The laser power was always kept <150 µW to avoid selective chemical alteration. Due to the often-varying cyst surface topography, optimal signal intensities could only be recorded by refocusing the laser prior to each measurement. This was only performed for discrete point measurements, not for line and array scans. The signal intensity differences were minimized during data processing by using vector normalization. Spectra with low SNRs were excluded as outliers in further analyses.

4. DISCUSSION

4.1 Chemical variability of dinosporin, spectrochemical classification and resemblance to other resistant biomacromolecules

The wide range of principal component scores for different modern cyst taxa in a two-dimensional PCA plot of the ATR micro-FTIR dataset reveals a relatively large degree of chemical variability in their cyst walls (Figure 1c–d, Figure 2), which is supported by the large variance explained by the first to components (PC1: 73.5%, PC2: 12.8%, together: 86.3%). However, when looking at the individual spectra, some specific molecular components appear ubiquitous in all specimens: there is proof for hydrogen (hydroxyl) bonding (bands “1A” and “1D”), amide groups (bands “1B–C” and “1E”) and β-1,4-linked

374 polysaccharides (bands “1F–G”) (Figure 1a–b, Table 1), suggesting that the backbone of
375 dinosporin is a heavily cross-linked, N-containing, cellulose-like macromolecule. These
376 findings support the earlier idea of dinosporin being a highly resistant, carbohydrate-based
377 compound, now with added support for the presence of proteinaceous – and/or (poly)peptide
378 – materials built into the cyst wall, rather than as possible external contaminants (Versteegh et
379 al., 2012). The spectrochemical similarity to cellulose was previously shown (Bogus et al.,
380 2014; Versteegh et al., 2012) and is also supported here (Figure 1a, Table 1). As armored
381 dinoflagellates can biosynthesize cellulosic compounds in the form of thecal plates (e.g.,
382 Janouškovec et al., 2017 and refs herein) or division cysts (Mertens et al. 2021), it is not
383 surprising that similar macromolecules also occur in the walls of their resting cysts. Besides
384 the ubiquitous cellulose-like backbone (CLB) and its associated absorption bands, sometimes
385 additional molecular components can be identified when looking into more detail at the
386 spectra. The result is a proposed classification into four spectrochemical groups, each group
387 defined by several characteristic absorption bands (Figure 1, Table 1).
388
389 *4.1.1 Group 1: transparent cysts with basic dinosporin*
390
391 This group includes transparent gonyaulacalean cysts belonging to the genera
392 *Impagidinium*, *Lingulodinium*, *Operculodinium*, *Polysphaeridium*, *Spiniferites*, *Tectatodinium*
393 and *Tuberculodinium*) (Plate S1). The spectra show mainly CLB absorption bands (bands
394 1A–G) together with weak carbonyl (1720–1695 cm^{-1}) and carbohydrate-like methylene
395 (2955–2845 and 1445–1350 cm^{-1}) bands (Figure 1a–b, Table 1). We deem these cysts to be
396 composed of the most basic type of dinosporin, which is further supported by the results of
397 bleaching experiments (see paragraph 4.2). The observed inclusion of other specific

molecular compounds to this basic dinosporin led to the erection of three other spectrochemical groups, each with their associated dinosporin types.

4.1.2 Group 2: colored cysts

Group 2 includes peridinialean (*Archaeperidinium*, *Brigantedinium*, *Dubridinium*, *Echinidinium*, *Lejeunecysta*, *Parvodinium*, *Peridinium*, *Qia*, *Quinquecuspis*, *Selenopemphix*, *Trinovantedinium* and *Votadinium*) and gymnodinialean (*Gymnodinium* and *Polykrikos*) cysts (Plates S2–S3) which all have colored (usually light to dark brown) walls. Their characteristic absorption bands can be associated with the presence of secondary amines (bands 2A–C; Figure 1a–b, Table 1), which we deem to originate from the pigment(s) present in their cyst walls. Based on the strong similarities with a spectrum of a *Sepia officinalis* eumelanin standard and the bleaching behavior of colored cyst due to oxidizing agents (see paragraph 4.2), we consider that the pigment responsible for the coloration of some dinocysts is strongly similar or possibly identical to eumelanin. In summary, we argue that the type of dinosporin present in colored cysts is essentially basic dinosporin (as identified in group 1) with an additional pigment which is likely eumelanin.

4.1.3 Group 3: aromatic cysts

Group 3 includes only one transparent, peridinialean cyst taxon, *Trinovantedinium applanatum* (Plate S3), with characteristic absorption bands attributable to the presence of aromatic rings (bands 3A–D; Figure 1a–b, Table 1). This unusual type of dinosporin has been reported for *T. applanatum* before (Gurdebeke et al., 2020; Meyvisch et al., 2022), but has to date not been found in any other dinocyst taxa. Analogous to findings by Gurdebeke et al.

(2020), our spectra also show an absence of aromatic bands for closely related and light brown-colored *Trinovantedinium pallidifulvum* cysts (Mertens et al., 2017). The aromatic dinosporin in *T. applanatum* also shows similarities with sporopollenin, another resistant biomacromolecule which is known to be partially composed of aromatic building blocks (i.e., *p*-coumaric acids; Li et al., 2019), and which has been studied much more extensively than dinosporin via spectrochemical methods (e.g., Jardine et al., 2021 and refs herein). Comparable characteristic aromatic absorption bands are present in a spectrum of a *Pinus* sp. pollen (Figure 1a), though the absence of CLB bands indicates that sporopollenin is not identical to the aromatic macromolecule found in *T. applanatum*. In summary, we argue that the type of dinosporin present in *T. applanatum* is essentially basic dinosporin (as identified in group 1) with addition of aromatic, sporopollenin-like molecular components.

Sporopollenin is known to provide protection against UV-induced oxidation and microbial degradation (Blokker et al., 2005; Rozema et al., 2001), therefore a similar aromatic macromolecule, like the one identified in *T. applanatum*, could have comparable functions. It remains a mystery why it is currently only found in this cosmopolitan species (e.g., Zonneveld et al., 2013), but it might be connected to *T. applanatum*'s unusual transparency with respect to its heterotrophic life mode (see paragraph 4.2.3 for further elaboration). Interestingly, a terrestrial UV-B (280–315 nm) proxy has been established based on the intensity of a prominent aromatic absorption band (~1510 cm^{-1}) in FTIR spectra of pollen and spores (e.g., Jardine et al. 2017 and refs herein). As this band is also present in spectra of *T. applanatum*, its potential applicability as a marine UV-B proxy should be further investigated via laboratory-controlled culture experiments, followed by ATR micro-FTIR spectroscopy and spectroscopy in the ultraviolet and visible ranges. As heterotrophic dinoflagellates are difficult to culture in general, the main challenge here lies in acquiring

448 sufficient cell and cyst volumes. Perhaps the presence of 1510 cm^{-1} band in *T. applanatum*,
449 together with other sharp bands at 1180–1250 and 1610 cm^{-1}, might suggest the presence of
450 lignin (Boeriu et al., 2004), which might also be present in pollen (Kenđel & Zimmermann,
451 2020).
452
453 *4.1.4 Group 4: aliphatic cysts*
454
455 Group 4 includes two transparent, peridiniacean cyst taxa, *Fusiperidinium*
456 *wisconsinense* and *Peridinium limbatum* (Plate S3), from a freshwater lake (Plastic Lake,
457 Table S1), which show characteristic, unusually prominent aliphatic absorption bands (bands
458 4A–D; Figure 1a–b, Table 1). As such, this type of dinosporin shows similarities with
459 algaenan (*Botryococcus braunii* algaenan extract; Figure 1a), another resistant
460 biomacromolecule known to be composed of long hydrogenated C chains (Kodner et al., 2009
461 and refs herein), and which is most often found in spores and resting stages of freshwater
462 organisms (Gelin et al., 1999; Versteegh & Blokker, 2004). Though the absence of CLB
463 bands in the *Botryococcus* spectrum indicates that algaenan is not identical to the
464 macromolecule found in the walls of *F. wisconsinense* and *P. limbatum*. Interestingly, spectra
465 of dark brown-colored *Parvodinium umbonatum* cysts, isolated from the same freshwater lake
466 sample, are classified within spectrochemical group 2 and show no unusually strong aliphatic
467 absorption bands. In summary, we argue that the type of dinosporin present in *F.*
468 *wisconsinense* and *P. limbatum* is essentially basic dinosporin (as identified in group 1) with
469 addition of aliphatic, algaenan-like molecular components.
470
471 In extant algae, algaenans have almost exclusively been reported for freshwater
472 species (Versteegh & Blokker, 2004). Reported instances are from spores and resting stages

473 of Eustigmatophyta and Chlorophyta (the latter occur predominantly in freshwater
474 environments; Matsunaga et al., 2005), and no algaenans have (yet) been found in
475 Bacillariophyta and Haptophyta (e.g., Versteegh and Blokker, 2004). Algaenan was also
476 reported from vegetative cells of the marine dinoflagellate *Gymnodinium catenatum* (Gelin et
477 al., 1999), though this represents only a single instance. Algaenan likely serves as a protective
478 compound providing resistance to chemical and biological attack, environmental stress
479 (particularly to desiccation), and structural reinforcement of cell and spore walls (e.g., Kodner
480 et al., 2009; Versteegh and Riboulleau, 2010). The aliphatic compounds identified in *F.*
481 *wisconsinense* and *P. limbatum* might have similar biological functions, perhaps also allowing
482 these cysts to better survive periods of prolonged UV exposure and/or drought. However,
483 experiments on terrestrial, stress-tolerant algae have shown only a weak correlation between
484 tolerance to environmental extremes and algaenan production, with only a few species being
485 able to synthesize the biopolymer, suggesting that their resistance to desiccation was mainly
486 due to their unusually thick cell walls (Kodner et al., 2009). Surprisingly, ATR micro-FTIR
487 spectra of cysts of *Parvodinium umbonatum* contain no large, characteristic aliphatic
488 absorption bands, and are very similar to those of other colored cysts in spectrochemical
489 group 2. As such, not all freshwater cysts analyzed in this study contain algaenan-like
490 components and neither do cysts of *G. catenatum*, in contrast to the report on their vegetative
491 counterparts (Gelin et al., 1999). Nevertheless, the common occurrence of algaenan in resting
492 stages of mostly freshwater microorganisms, suggests that it contributes significantly to the
493 survival potential of these lifeforms in such environments.
494
495 *4.2 Investigating the color of dinocyst walls*
496

Even though all analyzed colored cysts were grouped into one spectrochemical group (i.e., group 2), upon detailed investigation some small inter- and intraspecific chemical variability could be observed, mainly associated with changing intensities of a few specific absorption bands (bands 2A–C; Table 1, Figure 1, Figure 3). Visual color gradients (generally light to dark brown) were observed in colored cysts, sometimes even between specimens of the same species, which led us to hypothesize that this color variation could also be spectrally detected. To test this hypothesis, an educated guess was first made on a likely candidate pigment responsible for the coloration of dinocyst walls. A shortlist was created by combining molecular information retrieved from the detailed characterization of functional groups present in spectra of colored cysts, together with prior knowledge about common light to dark brown biological pigments known from other (micro)organisms. This led to the selection of eumelanin as a likely pigment candidate, its subsequent spectrochemical analysis and the idea to perform several bleaching experiments and analyses on certain cyst taxa.

4.2.1 Eumelanin: a likely pigment in colored dinocyst walls

Common biological pigments causing similar colors to those observed in colored dinocysts are yellow to red-brown melanin, found in higher animals, seeds of plants, protists, bacteria, and (spores of) fungi (Eisenman & Casadevall, 2012; Gao & Garcia-Pichel, 2011; Glagoleva et al., 2020; Plonka & Grabacka, 2006), and scytonemin, commonly present in the sheaths of cyanobacteria (Proteau et al., 1993). They both provide protection against harmful UV-A and UV-B light, other oxidizing agents, and ionizing radiation (Carletti et al., 2014; Proteau et al., 1993). Furthermore, many organisms, including some dinoflagellates, synthesize other UV-protective pigments called mycosporine-like amino acids (MAAs; e.g., Sinha et al., 2007), but which are not known to cause any visual coloration. In dinoflagellates,

these MAAs are known to accumulate in the cytoplasm or packed around UV-sensitive organelles (Laurion et al., 2004) and occur in species capable of forming both transparent (e.g., Vernet and Whitehead, 1996; Carreto et al., 2001; Flaim et al., 2014), and colored cysts (Vale, 2015). Interestingly, several studies report an unknown MAA (M-370) in *Gymnodinium catenatum* with an unknown color contribution and a strong absorption in the near-UV-A (340–400 nm; peak at 370 nm) (J. I. Carreto et al., 2005; Jeffrey et al., 1999; Vale, 2015). M-370 is currently only found in *G. catenatum*, which produces a colored cyst. Fossilized dinocysts also show variety in cyst wall colors similar to modern counterparts, though in several cases these might not be the result of in-situ pigmentation, but rather due to secondary geological processes like weathering-induced post-depositional oxidation (Traverse, 2007) and thermal maturation during diagenesis (Hartkopf-Fröder et al., 2015), which respectively induce carbonization and coalification processes.

Scytonemin was rapidly excluded from the shortlist as no evidence for C–N units associated with aromatic rings (N = C–C = C, ~1513 cm^{-1}) (Pandey et al., 2020) was found in the spectra of colored cysts (Figure 1a–b, Table 1). MAAs were also excluded due to them being essentially transparent and because it is unknown whether they also accumulate in outer, enveloping walls or layers of microorganisms. Different melanins exist, with the most common types being eumelanin and the S-containing pheomelanin. Less common types are N-free pyo- and allomelanin, known from bacteria, and neuromelanin, which is present in specific neuronal groups in human brain stems (Choi, 2021). All types other than eumelanin were excluded given the absence of characteristic S absorption bands and the presence of secondary amine bands in spectra of colored cysts, as well as the specific occurrence of neuromelanin. The spectra retrieved from a *Sepia officinalis* eumelanin standard contain several absorption bands which are also present in spectra of colored cysts, and which are

547 mainly associated with the presence of hydroxyl (OH) and carbonyl (C = O) groups,
548 carboxylic acids (COOH) and secondary amines (N– H) (Figure 1, Table 1). No evidence for
549 secondary amines is found in the spectra from transparent cysts analyzed in this study (Figure
550 1a–b, Table 1), suggesting that this functional group is exclusive to colored cysts and
551 originates from their constituting eumelanin pigmentation.
552
553 *4.2.2 Bleaching behavior of colored dinocysts in response to oxidation*
554
555 Melanins are known to bleach with oxidative agents such as H_2O_2 (Liu et al., 2013)
556 and UV-A light, with pheomelanin showing a slightly different photostainability than
557 eumelanin (Ou-Yang et al., 2004). For this reason, we have exposed several colored cysts to
558 high (non-natural) doses of one of these oxidative agents, expecting them to bleach rapidly
559 over time, which was indeed observed (Videos S1, S3–4). Subsequently, spectra were
560 recorded for a eumelanin standard and bleached specimens to monitor the bleaching-induced
561 molecular changes (Figure 3). The spectral data show a progressive bleaching gradient with
562 exposure time to oxidation in dark brown colored *Brigantedinium* sp. cysts, expressed as a
563 systematic reduction of the intensity of secondary amine absorption bands (Figure 3, spectra
564 ii–iv). This is best visible in the most prominent '2A band' (Figure 3, Table 1). The
565 incompletely H_2O_2-bleached specimen (Figure 3, spectrum iii) still shows some slight optical
566 coloration and more intense pigment-associated absorption bands when compared to the
567 thoroughly UV-A-bleached specimen (Figure 3, spectrum iv). The difference spectrum
568 (Figure 3, spectrum v) of unbleached and heavily bleached specimens shows large similarities
569 to that of the eumelanin standard (Figure 3, spectrum i), while the spectrum of the heavily
570 bleached specimen is quite similar to that of transparent cysts (Figure 3, spectrum vi). This

supports the idea of the presence of a CLB as a resistant macromolecular structure in the walls of dinocysts.

4.2.3 Possible functions of pigments in dinocyst walls

Eumelanin and related pigments provide protection against harmful UV radiation (Carletti et al., 2014), perhaps allowing colored cysts to survive longer in the upper water column or shallow-water sediments, to grow better in more shallow aquatic environments, or to occupy specific econiches. The slower bleaching of the red body inside a colored *Gymodinium catenatum* cyst (~5 mins) compared to that of a transparent *Pentapharsodinium dalei* cyst (~3 mins) could support this hypothesis (Videos S1 and S2). The penetration depth of UV light in water varies with the type of marine environment, but generally 90% is scattered and absorbed in the upper 10 (UV-B) to few 10's (UV-A) of meters (Tedetti & Sempéré, 2006), though low doses (much lower than the doses used here) can still be harmful to phytoplankton communities (Johnsen & Sosik, 2004). Since natural color gradients in dinocysts occur, it would be worth investigating whether these – as well as fluctuations in colored to transparent cyst ratios – might correlate with received environmental UV-A and UV-B fluxes. This likely is a complicated exercise for which aspects like cyst formation, deposition and transport need to be accounted for.

Pigments in dinocysts walls could well act as a sunscreen, because this passive – though inefficient (given the required mass and energy investments) – form of defense is often found in sensitive, immobile life cycle stages of microorganisms (Gao & Garcia-Pichel, 2011). Colored sunscreens in cyst walls perhaps provide additional protection to the cysts' cellular contents by compensating for the absence or lowered accumulations of MAAs in the

596 cytoplasm, or by complementing the absorption properties of specific MAAs internally
597 present. MAAs are known to protect against UV-inhibition of phytoplankton photosynthesis
598 (Day & Neale, 2002). Perhaps transparent organic-walled cysts do not need an enveloping
599 sunscreen layer as their corresponding, usually autotrophic, cells were able to internally
600 accumulate sufficiently large concentrations and suites of MAAs, which effectively protect
601 the entirety of the cellular contents from harmful radiation. This might explain the unusual
602 aromatic (i.e., capable of UV absorption) and transparent cyst wall of *Trinovantedinium*
603 *applanatum* (Figure 1a–b, Table 1), which could provide additional protection to compensate
604 for insufficient MAAs present in its corresponding, heterotrophic vegetative stage.
605 Surprisingly, while being able to form colored cysts, the MAA concentrations in
606 *Gymnodinium catenatum* can be 1–2 orders of magnitude larger than in transparent cyst-
607 producing species (Vale, 2015, 2018). Despite Vale (2015) currently being the only report of
608 the MAA profile of a colored cyst-producing species, it could suggest that the quality, rather
609 than the quantity of the suite of MAAs present in the cellular contents might be related to the
610 presence or absence of an enveloping, colored sunscreen layer. MAA profiles of colored
611 autotrophs (e.g., *Parvodinium umbonatum*) and heterotrophs (which are difficult to culture)
612 are needed to further explore the possible links between cellular MAA contents, trophic
613 affinities, and cyst wall pigmentation, and to investigate whether mixo- and heterotrophs can
614 acquire and accumulate certain MAAs through prey ingestion. The latter could be possible,
615 since common prasinophycean, dinoflagellate and diatom prey of thecate heterotrophs contain
616 MAAs (e.g., Jacobson and Anderson, 1986; Sinha et al., 2007). Other sunscreen functions
617 might be to contain active repair mechanisms associated with metabolic suppression during
618 the hypnozygote stage (e.g., Binder and Anderson 1990, Ellegaard and Ribeiro, 2018, Deng et
619 al. 2017), and/or to safeguard the breakdown of – perhaps colored cyst-specific – storage
620 compounds (i.e., lipid and starch globules). It is not excluded that dinocysts can build MAAs

621 into their cyst wall, similar to diatoms in their frustules (Ingalls et al., 2010), but this could
622 not be confirmed from the spectral data presented here, due to a lack of reference spectra from
623 MAA standards. Even if MAAs would be present in cyst walls, it might be that their
624 concentrations are below the detection limit of conventional ATR micro-FTIR spectroscopy
625 (~280 ppm, Lanzarotta, 2015).
626
627 *4.2.4 Influence of dinocyst color on its autofluorescence*
628
629 The autofluorescence of eumelanin is negligible (Nighswander-Rempel et al., 2005),
630 but can be induced by oxidation with H_2O_2 (Kayatz et al., 2001) and UV-A (Elleder &
631 Borovanský, 2001). Interestingly, during UV-A bleaching of a cyst of *Dubridinium* sp., a light
632 blue luminescent signal developed which was clearly observable after ~5 mins of bleaching
633 using a U-MWU2 Olympus fluorescent filter cube (Video S4). Though unlike the typical
634 yellow–green autofluorescence of oxidized melanin (Elleder & Borovanský, 2001; Kayatz et
635 al., 2001), a similar color was observed in UV-oxidized liquid melanin samples (Gallas &
636 Eisner, 1987), but no further explanation for this blue shift was provided. The inference of
637 trophic affinity through dinocyst autofluorescence (Brenner and Biebow, 2001) might be
638 biased because of the preference of heterotrophs to produce colored cysts. In other terms, the
639 reduced autofluorescence in inferred heterotrophs might perhaps be solely due to cyst wall
640 melanin inhibiting most of the detectable autofluorescent signals. Our observations support
641 this hypothesis as cysts of *Trinovantedinium applanatum* show autofluorescence, while those
642 of *Parvodinium umbonatum* do not. Other melanin-containing organic-walled palynomorphs
643 like fungal spores (Eisenman & Casadevall, 2012) and scolecodonts (Ehrlich, 2019) also
644 show reduced autofluorescence, while transparent forms like chlorococcalean,

prasinophycean, desmidiacean algae, zygnematacean cysts and cuticles of pollen and spores do not (Brenner and Biebow, 2001).

4.2.5 Differential morphological changes in dinocysts during oxidation

The loss of color in colored cysts and differential degradation of ornamentation of transparent and colored cysts due to oxidation creates issues with respect to their recognizability, as both morphological characteristics are important for the identification of cysts (Matsuoka & Fukuyo, 2000). A prime example is a colored cyst of *Archaeperidinium minutum* which, after UV-A bleaching, is no longer identifiable as such (Figure S1 and S2, Video S3). Here, the loss of delicate ornamentation might be a consequence of the packing of pigments on tegumentary layers of the already thin-walled species (Mertens et al., 2020), which is a common conformation of sunscreens (Gao & Garcia-Pichel, 2011). Contrastingly, the morphology of a cyst of *Pentapharsodinium dalei* is completely preserved, even after more than double the UV-A bleaching duration (Figure S1, Video S2). High magnitude photographs (1000 ×) of the UV-A-bleached cyst of *A. minutum* show that small protrusions of the transparent wall layer are present at the locations of where the processes used to be (Figure S2). This supports the hypothesis of structurally packed pigments in the cysts' outer wall layers, which in this case formed the majority of the process volume. A relatively thick outer pigment layer likely contributes significantly to the structural integrity of the cyst and when it is removed via oxidation what is left is a thin, though still resistant (i.e., consisting of a CLB), inner wall layer. Such a thin layer can be easily deformed or disintegrated, which could explain why cysts of *A. minutum* are only found in modern samples and why colored cysts in general preserve worse than their transparent counterparts which are built from generally thicker, resistant wall layers. Such a thin and easily deformable inner wall layer

perhaps also facilitates excystment and could be related to the generally shorter dormancy periods of colored cysts (e.g., <15 days for *Gymnodinium catenatum*; Figueroa et al., 2008) in comparison to thicker-walled transparent cysts (e.g., up to 6 months for *Alexandrium tamarense*; Fukuyo, 1982). As most modern peridinalean cysts are colored, this creates a preservational bias in favor of, typically transparent, gonyaulacalean cysts. This confirms previous observations made on modern cysts (Marret, 1993; Persson & Smith, 2022; Reid, 1977), and this bias is likely extrapolatable to the fossil record (Dale, 1976). It is therefore important to address the (possible) degree of oxidation of the sample in the case of quantitative dinocyst assemblage studies, what caused it and, more importantly, to prevent oxidative steps during sample processing. This matches previous recommendations by Mertens et al. (2009).

4.2.6 Concluding remark on the color of dinocyst walls

While we have shown that there exist many shared characteristics between the pigment in cyst walls and eumelanin, more specific methods such as Fontana-Masson melanin staining (Fontana, 1912; Kimura & McGinnis, 1998; Masson, 1928), M-INK immunolabeling (Yoshikawa-Murakami et al., 2020) and/or transcriptomics should be applied for a more definitive confirmation of its presence. Many microorganisms, including dinoflagellates, use polyketide synthases (PKSs) to produce pigments (including melanins), antibiotics, toxins, and other products of intermediate metabolism (Plonka & Grabacka, 2006). Though melanin synthesis in dinoflagellates is not reported yet, a potentially melanogenic pathway might be present.

4.3 Re-evaluation of dinocyst composition as a proxy for trophic affinity

In contrast to what was previously assumed by Bogus et al. (2014), our results show that N is present in the cyst walls of both auto- and heterotropic dinoflagellates, and their trophic affinities cannot be unambiguously inferred from the FTIR spectra of their associated cysts. The former is apparent from the presence of amide absorption bands in all spectra from the ATR dataset (Figure 1a–b, Table 1), the latter by the unusual positions of clusters of *Parvodinium umbonatum* (dark brown autotroph), and *Trinovantedinium applanatum* (transparent heterotroph) within or closer to the larger clusters of autotrophic and heterotrophic cysts, respectively (Figure 2). Furthermore, mixotrophic cysts do not have compositions intermediate to photoautotrophic and heterotrophic cysts but show a large spectrochemical variability; with (reddish-)brown cysts of *Gymnodinium nolleri/catenatum* being similar to other colored cysts (group 2), and transparent *Lingulodinium machaerophorum* being similar to other transparent cysts (group 1) (Figure 2). The trophic classification of Bogus et al. (2014) is based on the presence or absence of N absorption bands and the authors used a transflection micro-FTIR method, which was later shown to be the sampling method most prone to spectral distortion (i.e., band shifts and intensity modulations) (Meyvisch et al., 2022). Here we show that by using a more robust sampling method, a larger dataset including unusual taxa, and more in-depth data processing, N is present in all analyzed cysts and that pigmentation, rather than nutritional strategy, is a large contributor to the observed compositional diversity of dinosporin. This also implies that comparative morphology is the most unambiguous tool for inferring trophic affinities – and by extension the auto/heterotroph ratios – of fossil dinoflagellates (Penaud et al., 2018; Pospelova et al., 2006). Given the preference of modern heterotrophs to form colored cysts and the detectability of pigments in FTIR spectra, this method can still ambiguously assess the trophic affinity in most extant species (>95% of the species analyzed here), which can be valuable in

some cases. However, this assumption becomes more ambiguous when inferring the trophic affinities of fossil species and should be sufficiently contextualized and nuanced.

4.4 Chemical homogeneity of dinocyst walls

Only the uppermost ~1 µm of the compressed sample is probed by the shallowly penetrating evanescent IR beam when using the ATR micro-FTIR approach (Meyvisch et al., 2022; Milosevic, 2012). An ATR micro-FTIR spectrum only accurately represents the bulk composition of the entire specimen if all cyst wall layers are be chemically homogenous, which is a straightforward and fair assumption. To investigate chemical heterogeneity, hyperspectral images were recorded from individual cysts by using high spatial resolution methods like synchrotron transmission micro-FTIR (6×6 µm^2 spot size, IR beam fully penetrates the sample), and O-PTIR ($\sim 0.5 \times 0.5$ µm^2, IR beam penetrates a few µm into the sample; Freitas et al., 2021) spectroscopy (Reffner, 2018). Our results indicate that the compositions of the central bodies and ornamentations or (ant)apical horns are highly similar (i.e., the averaged spectra contain the same absorption bands) (Figure 4). This was the case for all taxa (modern and fossil) analyzed in this study. This implies that micro-FTIR (including ATR) and O-PTIR spectra derived from dinocysts analyzed here can be seen as representations of their bulk chemical compositions. The values of the standard deviations around the mean are generally higher in the spectra collected from processes (Figure 4b, spectrum i) than in those collected from the central body (Figure 4b, spectrum ii), which can be attributed to stronger, more complex scattering artifacts and lower SNRs for the former. The low SNR is indicated by the presence of background noise absorptions between 1000–900 cm^{-1} which are also present in the background spectrum (Figure 4b, spectrum iii). Some of the minor relative absorption band intensity differences in the O-PTIR spectra (Figure 4c)

might result from the fact that the shown spectral region was recorded as three separate bands, which were later mathematically merged (near 1510 and 1200 cm^{-1}) in the PTIR-studio software. It is important to note that scattering and interference artifacts are present in both the synchrotron transmission micro-FTIR and O-PTIR spectra, as they are collected by contact-free methods probing microparticles with irregular surface topographies and morphologies. Therefore, these spectra are not fully quantitative (Mayerhöfer et al., 2020; Pavlovetc et al., 2020), which might also explain some minor absorption band intensity differences between spectra of the taxa presented here.

Acknowledgements

The facility used for ATR micro-FTIR was funded by the Hercules Foundation (FWO, Flanders; FT-IMAGER project—AUGE/13/16). The bleaching experiments were carried out during a research stay at Ifremer LER BO (Concarneau, France) which was funded by an FWO grant for a short study visit abroad (file number: K210522N). The authors acknowledge SOLEIL synchrotron (Paris, France) for providing synchrotron radiation facilities (proposal ID "20201131"), as well as the mIRage O-PTIR spectrometer. Many thanks go out to Coralie André, for participating in the analyses at SOLEIL, and Nicolas Chomerat for helping with the UV-A bleaching experiments at Station Ifremer (Concarneau, France). The authors also acknowledge Eric Abadie, Elinor Andren, Coralie Connes, Mark Furze, Haifeng Gu, Luc Lebrun, Nathalie Malet, Francine McCarthy, Aya Morinaga, Lourdes Morquecho, Zivana Nincevic, Ana Pienkowski, Jessica Ray, Aouregan Terre Terrillon, Serdar Uzar, Gerard Versteegh, and Karin Zonneveld for providing sediment and rock samples used in this study. Laetitia Marchand and Wanjie Xie are thanked for respectively providing the cellulose and eumelanin standards. The associate editor, the two reviewers and Thomas Wong Hearing are

thanked for their constructive feedback on the manuscript. The author and co-authors declare no conflict(s) of interest.

References

Blokker, P., Yeloff, D., Boelen, P., Broekman, R. A., & Rozema, J. (2005). Development of a Proxy for Past Surface UV-B Irradiation: A Thermally Assisted Hydrolysis and Methylation py-GC/MS Method for the Analysis of Pollen and Spores. *Analytical Chemistry*, *77*(18), 6026–6031. https://doi.org/10.1021/ac050696k

Boeriu, C. G., Bravo, D., Gosselink, R. J. A., & van Dam, J. E. G. (2004). Characterisation of structure-dependent functional properties of lignin with infrared spectroscopy. *Industrial Crops and Products*, *20*(2), 205–218. https://doi.org/10.1016/j.indcrop.2004.04.022

Bogus, K., Harding, I. C., King, A., Charles, A. J., Zonneveld, K. A. F., & Versteegh, G. J. M. (2012). The composition and diversity of dinosporin in species of the *Apectodinium* complex (Dinoflagellata). *Review of Palaeobotany and Palynology*, *183*, 21–31. https://doi.org/10.1016/j.revpalbo.2012.07.001

Bogus, K., Mertens, K. N., Lauwaert, J., Harding, I. C., Vrielinck, H., Zonneveld, K. A. F., & Versteegh, G. J. M. (2014). Differences in the chemical composition of organic-walled dinoflagellate resting cysts from phototrophic and heterotrophic dinoflagellates. *Journal of Phycology*, *50*(2), 254–266. https://doi.org/10.1111/jpy.12170

Bravo, I., & Figueroa, R. (2014). Towards an Ecological Understanding of Dinoflagellate Cyst Functions. *Microorganisms*, *2*(1), 11–32. https://doi.org/10.3390/microorganisms2010011

Brenner, W. (1998). *Grundlagen und Anwendungsmöglichkeiten der Mikro-Absorptionsphotometrie für organisch-wandige Mikrofossilien*. GEOMAR Forschungszentrum für marine Geowissenschaften.

Brenner, W., & Biebow, N. (2001). Missing autofluorescence of recent and fossil dinoflagellate cysts - an indicator of heterotrophy? *Neues Jahrbuch Für Geologie Und Paläontologie - Abhandlungen*, *219*(1–2), 229–240. https://doi.org/10.1127/njgpa/219/2001/229

Callone, A. I., Carignan, M., Montoya, N. G., & Carreto, J. I. (2006). Biotransformation of mycosporine like amino acids (MAAs) in the toxic dinoflagellate *Alexandrium tamarense*. *Journal of Photochemistry and Photobiology B: Biology*, *84*(3), 204–212. https://doi.org/10.1016/j.jphotobiol.2006.03.001

Carletti, G., Nervo, G., & Cattivelli, L. (2014). Flavonoids and Melanins: A Common Strategy across Two Kingdoms. *International Journal of Biological Sciences*, *10*(10), 1159–1170. https://doi.org/10.7150/ijbs.9672

Carreto, J., Carignan, M., & Montoya, N. (2001). Comparative studies on mycosporine-like amino acids, paralytic shellfish toxins and pigment profiles of the toxic dinoflagellates *Alexandrium tamarense*, *A. catenella* and *A. minutum*. *Marine Ecology Progress Series*, *223*, 49–60. https://doi.org/10.3354/meps223049

Carreto, J. I., Carignan, M. O., & Montoya, N. G. (2005). A high-resolution reverse-phase liquid chromatography method for the analysis of mycosporine-like amino acids (MAAs) in marine organisms. *Marine Biology*, *146*(2), 237–252. https://doi.org/10.1007/s00227-004-1447-y

Cho, H.-J., Kim, C.-H., Moon, C.-H., & Matsuoka, K. (2003). Dinoflagellate Cysts in Recent Sediments from the Southern Coastal Waters of Korea. *Botanica Marina*, *46*(4). https://doi.org/10.1515/BOT.2003.030

Choi, K.-Y. (2021). Bioprocess of Microbial Melanin Production and Isolation. *Frontiers in Bioengineering and Biotechnology*, *9*. https://doi.org/10.3389/fbioe.2021.765110

Coates, J. (2006). Interpretation of Infrared Spectra, A Practical Approach. In *Encyclopedia of Analytical Chemistry* (pp. 10815–10837). John Wiley & Sons, Ltd. https://doi.org/10.1002/9780470027318.a5606

Colthup, N., Daly, L., & Wiberley, S. (1990). Introduction to Infrared and Raman Spectroscopy. In *Academic Press* (3rd ed.). Academic Press.

Dale, B. (1976). Cyst formation, sedimentation, and preservation: Factors affecting dinoflagellate assemblages in recent sediments from Trondheimsfjord, Norway. *Review of Palaeobotany and Palynology*, *22*(1), 39–60. https://doi.org/10.1016/0034-6667(76)90010-5

Day, T. A., & Neale, P. J. (2002). Effects of UV-B Radiation on Terrestrial and Aquatic Primary Producers. *Annual Review of Ecology and Systematics*, *33*(1), 371–396. https://doi.org/10.1146/annurev.ecolsys.33.010802.150434

de Leeuw, J. W., Versteegh, G. J. M., & van Bergen, P. F. (2006). Biomacromolecules of algae and plants and their fossil analogues. *Plant Ecology*, *182*(1–2), 209–233. https://doi.org/10.1007/s11258-005-9027-x

Demsar, J., Curk, T., Erjavec, A., Gorup, C., Hocevar, T., Milutinovic, M., Mozina, M., Polajnar, M., Toplak, M., Stajdohar, M., Lan, U., Lan, Z., Zbontar, J., Zitnik, M., & Blaz, Z. (2013). Orange: Data Mining Toolbox in Python. *Journal of Machine Learning Research*, *14*, 2349–2353.

Ehrlich, H. (2019). *Marine Biological Materials of Invertebrate Origin* (Vol. 13). Springer International Publishing. https://doi.org/10.1007/978-3-319-92483-0

Eisenman, H. C., & Casadevall, A. (2012). Synthesis and assembly of fungal melanin. *Applied Microbiology and Biotechnology*, *93*(3), 931–940. https://doi.org/10.1007/s00253-011-3777-2

Elleder, M., & Borovanský, J. (2001). Autofluorescence of melanins induced by ultraviolet radiation and near ultraviolet light. A histochemical and biochemical study. *The Histochemical Journal*, *33*(5), 273–281. https://doi.org/10.1023/A:1017925023408

Ellegaard, M., & Ribeiro, S. (2018). The long-term persistence of phytoplankton resting stages in aquatic 'seed banks.' *Biological Reviews*, *93*(1), 166–183. https://doi.org/10.1111/brv.12338

Evitt, W. R. (1985). Sporopollenin dinoflagellate cysts: Their morphology and interpretation. *American Association of Stratigraphic Palynologists Foundation*.

Fensome, R. A., Taylor, F. J. R., Norris, G., Sarjeant, W. A. S., Wharton, D. I., & Williams, G. L. (1993). A classification of fossil and living dinoflagellates. In *Micropaleontology Press Special Paper* (no. 7). American Museum of Natural History.

Figueroa, R., Bravo, I., Ramilo, I., Pazos, Y., & Moroño, A. (2008). New life-cycle stages of *Gymnodinium catenatum* (Dinophyceae): laboratory and field observations. *Aquatic Microbial Ecology*, *52*, 13–23. https://doi.org/10.3354/ame01206

Flaim, G., Obertegger, U., Anesi, A., & Guella, G. (2014). Temperature-induced changes in lipid biomarkers and mycosporine-like amino acids in the psychrophilic dinoflagellate *Peridinium aciculiferum*. *Freshwater Biology*, *59*(5), 985–997. https://doi.org/10.1111/fwb.12321

Fontana, A. (1912). No title. *Dermatol. Wochenshr.*, *50*(1003).

Freitas, R. O., Cernescu, A., Engdahl, A., Paulus, A., Levandoski, J. E., Martinsson, I., Hebisch, E., Sandt, C., Gouras, G. K., Prinz, C. N., Deierborg, T., Borondics, F., &

Klementieva, O. (2021). Nano-Infrared Imaging of Primary Neurons. *Cells*, *10*(10), 2559. https://doi.org/10.3390/cells10102559

Fukuyo, Y. (1982). The study for distribution of the cysts of paralytic shellfish poisoning causatives dinoflagellates. Report of technological development for red tide. *Showa*, *57*, 1–16.

Gallas, J. M., & Eisner, M. (1987). Fluorescence of melanin-dependence upon excitation wavelength and concentration. *Photochemistry and Photobiology*, *45*(5), 595–600. https://doi.org/10.1111/j.1751-1097.1987.tb07385.x

Gao, Q., & Garcia-Pichel, F. (2011). Microbial ultraviolet sunscreens. *Nature Reviews Microbiology*, *9*(11), 791–802. https://doi.org/10.1038/nrmicro2649

García-Oliva, O., Hantzsche, F. M., Boersma, M., & Wirtz, K. W. (2022). Phytoplankton and particle size spectra indicate intense mixotrophic dinoflagellates grazing from summer to winter. *Journal of Plankton Research*, *44*(2), 224–240. https://doi.org/10.1093/plankt/fbac013

Gelin, F., Volkman, J. K., Largeau, C., Derenne, S., Sinninghe Damsté, J. S., & de Leeuw, J. W. (1999). Distribution of aliphatic, nonhydrolyzable biopolymers in marine microalgae. *Organic Geochemistry*, *30*(2–3), 147–159. https://doi.org/10.1016/S0146-6380(98)00206-X

Glagoleva, A. Y., Shoeva, O. Y., & Khlestkina, E. K. (2020). Melanin Pigment in Plants: Current Knowledge and Future Perspectives. *Frontiers in Plant Science*, *11*. https://doi.org/10.3389/fpls.2020.00770

Gurdebeke, P. R. (2019). *Holocene dinoflagellate cysts and other palynomorphs from Northern Hemisphere estuaries*. Ghent University.

Gurdebeke, P. R., Mertens, K. N., Bogus, K., Marret, F., Chomérat, N., Vrielinck, H., & Louwye, S. (2018). Taxonomic Re-Investigation and Geochemical Characterization of Reid's (1974) Species of *Spiniferites* from Holotype and Topotype Material. *Palynology*, *42*(sup1), 93–110. https://doi.org/10.1080/01916122.2018.1465735

Gurdebeke, P. R., Mertens, K. N., Meyvisch, P., Bogus, K., Pospelova, V., & Louwye, S. (2021). *Hiddenocysta matsuokae* gen. et sp. nov. from the Holocene of Vancouver Island, British Columbia, Canada. *Palynology*, *45*(1), 103–114. https://doi.org/10.1080/01916122.2020.1750500

Gurdebeke, P. R., Mertens, K. N., Pospelova, V., Matsuoka, K., Li, Z., Gribble, K. E., Gu, H., Bogus, K., Vrielinck, H., & Louwye, S. (2020). Taxonomic revision, phylogeny, and cyst wall composition of the dinoflagellate cyst genus *Votadinium* Reid (Dinophyceae, Peridiniales, Protoperidiniaceae). *Palynology*, *44*(2), 310–335. https://doi.org/10.1080/01916122.2019.1580627

Hackett, J. D., Anderson, D. M., Erdner, D. L., & Bhattacharya, D. (2004). Dinoflagellates: a remarkable evolutionary experiment. *American Journal of Botany*, *91*(10), 1523–1534. https://doi.org/10.3732/ajb.91.10.1523

Hartkopf-Fröder, C., Königshof, P., Littke, R., & Schwarzbauer, J. (2015). Optical thermal maturity parameters and organic geochemical alteration at low grade diagenesis to anchimetamorphism: A review. *International Journal of Coal Geology*, *150–151*, 74–119. https://doi.org/10.1016/j.coal.2015.06.005

Head, M. J. (1996). Modern dinoflagellate cysts and their biological affinities. In J. Jansonius & D. C. McGregor (Eds.), *Palynology: principles and applications* (Issue July, pp. 1197–1248). American Association of Stratigraphic Palynologists Foundation.

Ingalls, A. E., Whitehead, K., & Bridoux, M. C. (2010). Tinted windows: The presence of the UV absorbing compounds called mycosporine-like amino acids embedded in the frustules of marine diatoms. *Geochimica et Cosmochimica Acta*, *74*(1), 104–115. https://doi.org/10.1016/j.gca.2009.09.012

[1]Date of submission: 31/07/2023

915 Inkscape Project. (2020). *Inkscape Project* (1.0.1). https://inkscape.org
916 Jacobson, D. M., & Anderson, D. M. (1986). Thecate heterotrophic dinoflagellates: feeding
917 behavior and mechanisms. *Journal of Phycology*, *22*(3), 249–258.
918 https://doi.org/10.1111/j.1529-8817.1986.tb00021.x
919 Janouškovec, J., Gavelis, G. S., Burki, F., Dinh, D., Bachvaroff, T. R., Gornik, S. G., Bright,
920 K. J., Imanian, B., Strom, S. L., Delwiche, C. F., Waller, R. F., Fensome, R. A., Leander,
921 B. S., Rohwer, F. L., & Saldarriaga, J. F. (2017). Major transitions in dinoflagellate
922 evolution unveiled by phylotranscriptomics. *Proceedings of the National Academy of*
923 *Sciences*, *114*(2). https://doi.org/10.1073/pnas.1614842114
924 Jardine, P. E., Hoorn, C., Beer, M. A. M., Barbolini, N., Woutersen, A., Bogota-Angel, G.,
925 Gosling, W. D., Fraser, W. T., Lomax, B. H., Huang, H., Sciumbata, M., He, H., &
926 Dupont-Nivet, G. (2021). Sporopollenin chemistry and its durability in the geological
927 record: an integration of extant and fossil chemical data across the seed plants.
928 *Palaeontology*, *64*(2), 285–305. https://doi.org/10.1111/pala.12523
929 Jeffrey, S., MacTavish, H., Dunlap, W., Vesk, M., & Groenewoud, K. (1999). Occurrence of
930 UVA- and UVB-absorbing compounds in 152 species (206 strains) of marine
931 microalgae. *Marine Ecology Progress Series*, *189*, 35–51.
932 https://doi.org/10.3354/meps189035
933 Jeong, H. J., Yoo, Y. du, Kim, J. S., Seong, K. A., Kang, N. S., & Kim, T. H. (2010). Growth,
934 feeding and ecological roles of the mixotrophic and heterotrophic dinoflagellates in
935 marine planktonic food webs. *Ocean Science Journal*, *45*(2), 65–91.
936 https://doi.org/10.1007/s12601-010-0007-2
937 Johnsen, S., & Sosik, H. (2004). Shedding Light on Light in the Ocean: New research is
938 illuminating an optically complex environment. *Oceanus Vol.43 No.2*, 1–5.
939 Kayatz, P., Thumann, G., Luther, T. T., Jordan, J. F., Bartz-Schmidt, K. U., Esser, P. J., &
940 Schraermeyer, U. (2001). Oxidation Causes Melanin Fluorescence. *Investigative*
941 *Ophthalmology & Visual Science*, *42*, 241–246.
942 Kenđel, A., & Zimmermann, B. (2020). Chemical Analysis of Pollen by FT-Raman and FTIR
943 Spectroscopies. *Frontiers in Plant Science*, *11*. https://doi.org/10.3389/fpls.2020.00352
944 Kimura, M., & McGinnis, M. R. (1998). Fontana-Masson-stained tissue from culture-proven
945 Mycoses. *Archives of Pathology & Laboratory Medicine*, *122*(12), 1107–1111.
946 https://www.proquest.com/scholarly-journals/fontana-masson-stained-tissue-culture-
947 proven/docview/212023388/se-2?accountid=11077
948 Kodner, R. B., Summons, R. E., & Knoll, A. H. (2009). Phylogenetic investigation of the
949 aliphatic, non-hydrolyzable biopolymer algaenan, with a focus on green algae. *Organic*
950 *Geochemistry*, *40*(8), 854–862. https://doi.org/10.1016/j.orggeochem.2009.05.003
951 Kokinos, J. P., Eglinton, T. I., Goñi, M. A., Boon, J. J., Martoglio, P. A., & Anderson, D. M.
952 (1998). Characterization of a highly resistant biomacromolecular material in the cell wall
953 of a marine dinoflagellate resting cyst. *Organic Geochemistry*, *28*(5), 265–288.
954 https://doi.org/10.1016/S0146-6380(97)00134-4
955 Lanzarotta, A. (2015). Approximating the Detection Limit of an Infrared Spectroscopic
956 Imaging Microscope Operating in an Attenuated Total Reflection (ATR) Modality:
957 Theoretical and Empirical Results for an Instrument Using a Linear Array Detector and a
958 1.5 Millimeter Germanium Hemisphere Internal Reflection Element. *Applied*
959 *Spectroscopy*, *69*(2), 205–214. https://doi.org/10.1366/14-07538
960 Laurion, I., Blouin, F., & Roy, S. (2004). Packaging of mycosporine-like amino acids in
961 dinoflagellates. *Marine Ecology Progress Series*, *279*, 297–303.
962 Li, Z., Pospelova, V., Kawamura, H., Luo, C., Mertens, K. N., Hernández-Almeida, I., Yin,
963 K., Wu, Y., Wu, H., & Xiang, R. (2020). Dinoflagellate cyst distribution in surface
964 sediments from the South China Sea in relation to hydrographic conditions and primary

productivity. *Marine Micropaleontology*, *159*, 101815. https://doi.org/10.1016/j.marmicro.2019.101815
Liu, C.-H., Lin, C.-H., Tsai, M.-J., Chen, W.-T., Chai, C.-Y., Huang, Y.-C., & Tsai, K.-B. (2013). Melanin Bleaching With Dilute Hydrogen Peroxide. *Applied Immunohistochemistry & Molecular Morphology*, *21*(3), 275–279. https://doi.org/10.1097/PAI.0b013e31826d81db
Lundholm, N., Churro, C., Fraga, S., Hoppenrath, M., Iwataki, M., Larsen, J., Mertens, K., Moestrup, Ø., & Zingone, A. (2022, November 21). *IOC-UNESCO Taxonomic Reference List of Harmful Micro Algae*. Https://Www.Marinespecies.Org/Hab.
Mangerud, G., Paterson, N. W., & Riding, J. B. (2019). The temporal and spatial distribution of Triassic dinoflagellate cysts. *Review of Palaeobotany and Palynology*, *261*, 53–66. https://doi.org/10.1016/j.revpalbo.2018.11.010
Marret, F. (1993). Les effects de l'acetolyse sur les assemblages des kystes de dinoflagelles. *Palynosciences*, *2*, 267–272.
Marshall, C. P., Carter, E. A., Leuko, S., & Javaux, E. J. (2006). Vibrational spectroscopy of extant and fossil microbes: Relevance for the astrobiological exploration of Mars. *Vibrational Spectroscopy*, *41*(2), 182–189. https://doi.org/10.1016/j.vibspec.2006.01.008
Masson, P. (1928). No title. *The American Journal of Pathology*, *4*(181).
Matsunaga, T., Takeyama, H., Miyashita, H., & Yokouchi, H. (2005). *Marine Microalgae* (pp. 165–188). https://doi.org/10.1007/b135784
Matsuoka, K., & Fukuyo, Y. (2000). Technical guide for modern dinoflagellate cyst study. *WESTPAC-HAB, Japan Society for the Promotion of Science*, *47*.
Matsuoka, K., Kawami, H., Nagai, S., Iwataki, M., & Takayama, H. (2009). Re-examination of cyst–motile relationships of *Polykrikos kofoidii* Chatton and *Polykrikos schwartzii* Bütschli (Gymnodiniales, Dinophyceae). *Review of Palaeobotany and Palynology*, *154*(1–4), 79–90. https://doi.org/10.1016/j.revpalbo.2008.12.013
Mayerhöfer, T. G., Pahlow, S., & Popp, J. (2020). The Bouguer-Beer-Lambert Law: Shining Light on the Obscure. *ChemPhysChem*. https://doi.org/10.1002/cphc.202000464
Mertens, K. N., Gu, H., Gurdebeke, P. R., Takano, Y., Clarke, D., Aydin, H., Li, Z., Pospelova, V., Shin, H. H., Li, Z., Matsuoka, K., & Head, M. J. (2020). A review of rare, poorly known, and morphologically problematic extant marine organic-walled dinoflagellate cyst taxa of the orders Gymnodiniales and Peridiniales from the Northern Hemisphere. *Marine Micropaleontology*, *159*, 101773. https://doi.org/10.1016/j.marmicro.2019.101773
Mertens, K. N., Gu, H., Takano, Y., Price, A. M., Pospelova, V., Bogus, K., Versteegh, G. J. M., Marret, F., Turner, R. E., Rabalais, N. N., & Matsuoka, K. (2017). The cyst-theca relationship of the dinoflagellate cyst *Trinovantedinium pallidifulvum* , with erection of *Protoperidinium lousianensis* sp. nov. and their phylogenetic position within the *Conica* group. *Palynology*, *41*(2), 183–202. https://doi.org/10.1080/01916122.2016.1147219
Mertens, K. N., Takano, Y., Meyvisch, P., Carbonell-Moore, M. C., Chomérat, N., Bogus, K., & Leitão, M. (2021a). Morpho-molecular and spectroscopic characterization of the freshwater dinoflagellate *Unruhdinium penardii* var. *robustum* (Kryptoperidiniaceae, Peridiniales), blooming in the Loir River, France. *Nova Hedwigia*, *112*(3–4), 283–306. https://doi.org/10.1127/nova_hedwigia/2021/0633
Mertens, K. N., Takano, Y., Meyvisch, P., Carbonell-Moore, M. C., Chomérat, N., Bogus, K., & Leitão, M. (2021b). Morpho-molecular and spectroscopic characterization of the freshwater dinoflagellate unruhdinium penardii var. Robustum (kryptoperidiniaceae, peridiniales), blooming in the loir river, France. *Nova Hedwigia*, *112*(3–4). https://doi.org/10.1127/nova_hedwigia/2021/0633

Mertens, K. N., Verhoeven, K., Verleye, T., Louwye, S., Amorim, A., Ribeiro, S., Deaf, A. S., Harding, I. C., De Schepper, S., González, C., Kodrans-Nsiah, M., De Vernal, A., Henry, M., Radi, T., Dybkjaer, K., Poulsen, N. E., Feist-Burkhardt, S., Chitolie, J., Heilmann-Clausen, C., … Young, M. (2009). Determining the absolute abundance of dinoflagellate cysts in recent marine sediments: The *Lycopodium* marker-grain method put to the test. *Review of Palaeobotany and Palynology*, *157*(3–4), 238–252. https://doi.org/10.1016/j.revpalbo.2009.05.004

Meyvisch, P., Gurdebeke, P. R., Vrielinck, H., Mertens, K. N., Versteegh, G., & Louwye, S. (2022). Attenuated Total Reflection (ATR) Micro-Fourier Transform Infrared (Micro-FT-IR) Spectroscopy to Enhance Repeatability and Reproducibility of Spectra Derived from Single Specimen Organic-Walled Dinoflagellate Cysts. *Applied Spectroscopy*, *76*(2). https://doi.org/10.1177/00037028211041172

Milosevic, M. (2012). *Internal Reflection and ATR Spectroscopy*. John Wiley & Sons, Inc. https://doi.org/10.1002/9781118309742

Nighswander-Rempel, S. P., Riesz, J., Gilmore, J., & Meredith, P. (2005). A quantum yield map for synthetic eumelanin. *The Journal of Chemical Physics*, *123*(19), 194901. https://doi.org/10.1063/1.2075147

Ou-Yang, H., Stamatas, G., & Kollias, N. (2004). Spectral Responses of Melanin to Ultraviolet A Irradiation. *Journal of Investigative Dermatology*, *122*(2), 492–496. https://doi.org/10.1046/j.0022-202X.2004.22247.x

Pandey, A., Pathak, J., Singh, D. K., Ahmed, H., Singh, V., Kumar, D., & Sinha, R. P. (2020). Photoprotective role of UV-screening pigment scytonemin against UV-B-induced damages in the heterocyst-forming cyanobacterium *Nostoc* sp. strain HKAR-2. *Brazilian Journal of Botany*, *43*(1), 67–80. https://doi.org/10.1007/s40415-020-00589-5

Pavlovetc, I. M., Podshivaylov, E. A., Frantsuzov, P. A., Hartland, G. v., & Kuno, M. K. (2020). Quantitative infrared photothermal microscopy. In I. Gregor, R. Erdmann, & F. Koberling (Eds.), *Single Molecule Spectroscopy and Superresolution Imaging XIII* (p. 41). SPIE. https://doi.org/10.1117/12.2545159

Penaud, A., Hardy, W., Lambert, C., Marret, F., Masure, E., Servais, T., Siano, R., Wary, M., & Mertens, K. N. (2018). Dinoflagellate fossils: Geological and biological applications. *Revue de Micropaleontologie*, *61*(3–4), 235–254. https://doi.org/10.1016/j.revmic.2018.09.003

Persson, A., & Smith, B. C. (2022). Preservation of Dinoflagellate Cysts in Different Oxygen Regimes: Differences in Cyst Survival between Oxic and Anoxic Natural Environments. *Phycology*, *2*(4), 384–418. https://doi.org/10.3390/phycology2040022

Plonka, P. M., & Grabacka, M. (2006). Melanin synthesis in microorganisms - biotechnological and medical aspects. *Acta Biochimica Polonica*, *53*(3), 429–443.

Pollingher, U. (1987). Freshwater ecosystems. In F. J. R. Taylor (Ed.), *Bot Monogr 21: The biology of dinoflagellates* (pp. 502–529).

Pospelova, V., Pedersen, T. F., & de Vernal, A. (2006). Dinoflagellate cysts as indicators of climatic and oceanographic changes during the past 40 kyr in the Santa Barbara Basin, southern California. *Paleoceanography*, *21*(2), n/a-n/a. https://doi.org/10.1029/2005PA001251

Proteau, P. J., Gerwick, W. H., Garcia-Pichel, F., & Castenholz, R. (1993). The structure of scytonemin, an ultraviolet sunscreen pigment from the sheaths of cyanobacteria. *Experientia*, *49*(9), 825–829. https://doi.org/10.1007/BF01923559

Reffner, J. A. (2018). Advances in Infrared Microspectroscopy and Mapping Molecular Chemical Composition at Submicrometer Spatial Resolution. *Spectroscopy*, *33*(9), 12–17.

Reid, P. C. (1977). Peridiniacean and glenodiniacean dinoflagellate cysts from the British Isles. *Nova Hedwigia*, *29*, 429–463.
Rodrigues, R. V. (2022). *Ecology of cyst producing dinoflagellates*. Goa University.
Rozema, J., Broekman, R. A., Blokker, P., Meijkamp, B. B., de Bakker, N., van de Staaij, J., van Beem, A., Ariese, F., & Kars, S. M. (2001). UV-B absorbance and UV-B absorbing compounds (para-coumaric acid) in pollen and sporopollenin: the perspective to track historic UV-B levels. *Journal of Photochemistry and Photobiology B: Biology*, *62*(1–2), 108–117. https://doi.org/10.1016/S1011-1344(01)00155-5
Schnepf, E., & Elbrächter, M. (1992). Nutritional strategies in dinoflagellates. *European Journal of Protistology*, *28*(1), 3–24. https://doi.org/10.1016/S0932-4739(11)80315-9
Sinha, R. P., Singh, S. P., & Häder, D.-P. (2007). Database on mycosporines and mycosporine-like amino acids (MAAs) in fungi, cyanobacteria, macroalgae, phytoplankton and animals. *Journal of Photochemistry and Photobiology B: Biology*, *89*(1), 29–35. https://doi.org/10.1016/j.jphotobiol.2007.07.006
Smayda, T. J. (2002). Adaptive Ecology, Growth Strategies and the Global Bloom Expansion of Dinoflagellates. *Journal of Oceanography*, *58*(2), 281–294. https://doi.org/10.1023/A:1015861725470
Stoecker, D. K. (1999). Mixotrophy among Dinoflagellates. *The Journal of Eukaryotic Microbiology*, *46*(4), 397–401. https://doi.org/10.1111/j.1550-7408.1999.tb04619.x
Taylor, F. J. R. (1987). Ecology of dinoflagellates. *The Biology of Dinoflagellates*. https://cir.nii.ac.jp/crid/1570009750623263360.bib?lang=ja
Taylor, F. J. R., Hoppenrath, M., & Saldarriaga, J. F. (2008). Dinoflagellate diversity and distribution. *Biodiversity and Conservation*, *17*(2), 407–418. https://doi.org/10.1007/s10531-007-9258-3
Team, Rs. (2020). *RStudio; Integrated Development Environment for R*. Rstudio, PCB. http://www.rstudio.com
Tedetti, M., & Sempéré, R. (2006). Penetration of Ultraviolet Radiation in the Marine Environment. A Review. *Photochemistry and Photobiology*, *82*(2), 389. https://doi.org/10.1562/2005-11-09-IR-733
Toplak, M., Read, S. T., Sandt, C., & Borondics, F. (2021). Quasar: Easy Machine Learning for Biospectroscopy. *Cells*, *10*(9), 2300. https://doi.org/10.3390/cells10092300
Traverse, A. (2007). Paleogene Palynology. In *Paleopalynology* (pp. 391–426). Springer Netherlands. https://doi.org/10.1007/978-1-4020-5610-9_14
Vale, P. (2015). Effects of light quality and nutrient availability on accumulation of mycosporine-like amino acids in *Gymnodinium catenatum* (Dinophycea). *Journal of Photochemistry and Photobiology B: Biology*, *143*, 20–29. https://doi.org/10.1016/j.jphotobiol.2014.12.016
Vale, P. (2018). Impact of light quality and space weather in *Alexandrium catenella* (Dinophyceae) cultures. *Life Sciences in Space Research*, *19*, 1–12. https://doi.org/10.1016/j.lssr.2018.07.002
Versteegh, G. J. M., & Blokker, P. (2004). Resistant macromolecules of extant and fossil microalgae. *Phycological Research*, *52*(4), 325–339. https://doi.org/10.1111/j.1440-183.2004.00361.x
Versteegh, G. J. M., Blokker, P., Bogus, K., Harding, I. C., Lewis, J., Oltmanns, S., Rochon, A., & Zonneveld, K. A. F. (2012). Infra red spectroscopy, flash pyrolysis, thermally assisted hydrolysis and methylation (THM) in the presence of tetramethylammonium hydroxide (TMAH) of cultured and sediment-derived *Lingulodinium polyedrum* (Dinoflagellata) cyst walls. *Organic Geochemistry*, *43*, 92–102. https://doi.org/10.1016/j.orggeochem.2011.10.007

Versteegh, G. J. M., Blokker, P., Marshall, C., & Pross, J. (2007). Macromolecular composition of the dinoflagellate cyst *Thalassiphora pelagica* (Oligocene, SW Germany). *Organic Geochemistry*, *38*(10), 1643–1656. https://doi.org/10.1016/j.orggeochem.2007.06.007

Versteegh, G. J. M., Houben, A. J. P., & Zonneveld, K. A. F. (2020). Better molecular preservation of organic matter in an oxic than in a sulfidic depositional environment: Evidence from *Thalassiphora pelagica* (Dinoflagellata, Eocene) cysts. *Biogeosciences*, *17*(13), 3545–3561. https://doi.org/10.5194/bg-17-3545-2020

Versteegh, G. J. M., & Riboulleau, A. (2010). An organic geochemical perspective on terrestrialization. *Geological Society, London, Special Publications*, *339*(1), 11–36. https://doi.org/10.1144/SP339.3

Wall, D., & Dale, B. (1968). Modern dinoflagellate cysts and the evolution of the Peridiniales. *Micropaleontology*, *14*(3), 265–304.

Yoshikawa-Murakami, C., Mizutani, Y., Ryu, A., Naru, E., Teramura, T., Homma, Y., & Fukuda, M. (2020). A Novel Method for Visualizing Melanosome and Melanin Distribution in Human Skin Tissues. *International Journal of Molecular Sciences*, *21*(22), 8514. https://doi.org/10.3390/ijms21228514

Zonneveld, K. A. F., Marret, F., Versteegh, G. J. M., Bogus, K., Bonnet, S., Bouimetarhan, I., Crouch, E., de Vernal, A., Elshanawany, R., Edwards, L., Esper, O., Forke, S., Grøsfjeld, K., Henry, M., Holzwarth, U., Kielt, J.-F., Kim, S.-Y., Ladouceur, S., Ledu, D., … Young, M. (2013). Atlas of modern dinoflagellate cyst distribution based on 2405 data points. *Review of Palaeobotany and Palynology*, *191*, 1–197. https://doi.org/10.1016/j.revpalbo.2012.08.003

Captions

Figures

Figure 1. Panels (a) and (b) show average ATR micro-FTIR spectra (solid lines) of the erected spectrochemical groups and their characteristic absorption bands (grey rectangles, Table 1). Dashed lines in panel (a) represent comparable compounds, and the colored region around the solid line visualizes the standard deviation. The *Botryococcus braunii* algaenan spectrum is reproduced from Marshall et al. (2006) with permission from the authors. In panel (b) dashed lines represent the second derivatives of the average spectrum. Panel (c) shows a PCA plot of all ATR micro-FTIR spectra of dinocysts from surface sediment samples analyzed for this

study, colored in their assigned spectrochemical group, and with addition of a few additional spectra (black stars). Panel (d) shows the PCA loadings of the plot show in panel (c).

Figure 2. Shows the same PCA plot as in Figure 1c, now colored by trophic affinity, while the assigned, erected spectrochemical groups are represented as different symbols. The outlined groups (dashed lines) are further discussed in the text.

Figure 3. ATR micro-FTIR spectra showing the results of bleaching experiments on colored dinocysts. Dashed lines represent the second derivatives of the spectra shown here. The assignments of characteristic absorption bands (grey rectangles) can be found in Table 1.

Figure 4. Panel (a) shows a Coniacian–Santonian dinocyst specimen (*Valensiella foucheri*) analyzed via synchrotron transmission micro-FTIR spectroscopy. Each grey dot represents the center of a measurement using a square aperture with the dimension indicated on the figure. Via colored overlays, the specimen is subdivided into a central body, processes and background. Panel (b) shows the average spectra (solid lines) and standard deviations (colored regions) retrieved from the specimen presented in panel (a). Panel (c) shows average O-PTIR spectra retrieved from the central bodies (solid lines) and processes or antapical horns (dashed lines) of several dinocyst specimens from modern surface sediments. Scale bar = 20 µm.

Tables

Table 1. Overview of group frequencies identified from the ATR micro-FTIR spectra of dinocysts from modern surface sediments, with an indication of characteristic absorption

bands for each erected spectrochemical group (Figure 1a–b). VS = very strong, S = strong, M = medium, W = weak, A = absent. Absorption band identifications are based on Bogus et al. (2014), Coates (2006), Colthup et al. (1990) and Meyvisch et al. (2022).

Supplementary figures

Figure S1. Shows the effects of UV-A bleaching on the morphology of an initially colored (*Archaeperidinium minutum*) and initially transparent (*Pentapharsodinium dalei*) cyst.

Figure S2. Shows the presence of small protrusions (red arrows) of the resistant and transparent inner wall layer of a UV-A bleached cyst of *Archaeperidinium minutum* which are located at the locations where the processes used to be, prior to bleaching.

Figure S3. Shows the areas analyzed with O-PTIR spectroscopy from the cyst specimens presented in Figure 4c (each blue or red square represents a measurement point). The corresponding spectral data is available in Table S5.

Supplementary plates

Plate S1. Selection of modern dinocysts isolated from surface sediments, analyzed via ATR micro-FTIR spectroscopy and assigned to spectrochemical group 1 ('transparent cysts'; 1–28). 1. *Impagidinium variaseptum* (Isla San José). 2. *Lingulodinium machaerophorum* (Izmir Bay, Aegean Sea). 3. *Lingulodinium machaerophorum* (Aveiro, Rua da Forta da Barra). 4. *Lingulodinium machaerophorum* (Qinhuangdao, Bohai Sea). 5. *Operculodinium lapazense* (Isla San José). 6. *Polysphaeridium zoharyi* (Isla San José). 7. Cyst of *Protoceratium*

1198 *reticulatum* (Avafjärden, Gulf of Bothnia, Baltic Sea). 8. Cyst of *Protoceratium reticulatum*
1199 (Izmir Bay, Aegean Sea). 9. Cyst *of Protoceratium reticulatum* (Diana Lagoon, Corsica) . 10.
1200 Cyst of *Protoceratium reticulatum* (Lancaster Sound, Bylot Island). 11. *Spiniferites bentorii*
1201 (Isla San José). 12. *Spiniferites bentorii* (Diana Lagoon, Corsica). 13. *Spiniferites bentorii*
1202 (Izmir Bay, Aegean Sea). 14. *Spiniferites bentorii* (Pantan Bay). 15. *Spiniferites* cf.
1203 *membranaceus* (Isla San José). 16. *Spiniferites* cf. *ristingensis* (Izmir Bay). 17. *Spiniferites*
1204 *hyperacanthus* (Qinhuangdao, Bohai Sea). 18. *Spiniferites membranaceus*? (Wadden Sea). 19.
1205 *Spiniferites pseudodelicatus* (Qinhuangdao, Bohai Sea). 20. *Spiniferites ramosus* (Olhão
1206 Port). 21 *Spiniferites ramosus*? (Qinhuangdao, Bohai Sea). 22. *Spiniferites ristingensis* (Olhão
1207 Port). 23–24. *Spiniferites* sp. A (Isla San José). 25-27. *Tectatodinium pelitum* (Isla San José).
1208 28. *Tuberculodinium vancampoae* (Isla San José). Scale bar = 20 µm. More info on the
1209 samples and analyzed specimens can be found in Tables S1 and S3.
1210
1211 Plate S2. Selection of modern dinocysts isolated from surface sediments, analyzed via ATR
1212 micro-FTIR spectroscopy and assigned to spectrochemical group 2 (‘colored cysts’; 1–28). 1.
1213 *Archaeperidinium* sp. (Qinhuangdao, Bohai Sea). 2. *Brigantedinium majusculum* (Wadden
1214 Sea). 3. *Brigantedinium simplex* (Qinhuangdao, Bohai Sea). 4. *Brigantedinium* sp. sensu Cho
1215 et al. 2003 (Isla San José). 5. *Brigantedinium* sp. (Isla San José). 6. *Brigantedinium* sp.
1216 (Ōmura Bay, East China Sea). 7. *Brigantedinium* sp. (Pantan Bay). 8. *Brigantedinium* sp.
1217 (Thau Lagoon, Gulf of Lyon). 9. *Brigantedinium* sp. (Myntevikshavet). 10. *Brigantedinium*
1218 sp. (Xiamen Bay, Fujian). 11. Cyst of *Dubdridinium* sp. (Ōmura Bay, East China Sea). 12.
1219 Cyst of *Dubridinium* sp. (Aveiro, Rua da Forta da Barra). 13. Cyst of *Dubridinium* sp.
1220 (Qinhuangdao, Bohai Sea). 14. *Echinidinium bispiniformum* (Xiamen Bay, Fujian). 15.
1221 *Echinidinium* sp. (Izmir Bay, Aegean Sea). 16. *Gymnodinium nolleri/catenatum* (Diana
1222 Lagoon). 17. *Gymnodinium nolleri/catenatum* (Pantan Bay). 18. *Gymnodinium*

nolleri/catenatum (Olhão Port). 19. *Gymnodinium nolleri/catenatum* (Wadden Sea). 20. *Gymnodinium nolleri/microreticulatum* (Izmir Bay, Aegean Sea). 21-23. *Lejeunecysta* cf. *communis/pulchra/diversiforma*? (Qinhuangdao, Bohai Sea). 24. *Lejeunecysta epidoma*? (Qinhuangdao, Bohai Sea). 25. *Lejeunecysta oliva* (Wadden Sea). 26–27. *Parvodinium umbonatum* (Plastic Lake). Scale bar = 20 µm. More info on samples and analyzed specimens can be found in Tables S1 and S3.

Plate S3. Selection of modern dinocysts isolated from surface sediments, analyzed via ATR micro-FTIR spectroscopy and assigned to spectrochemical groups 2 ('colored cysts'; 1–22), 3 ('aromatic cysts'; 23–24), and 4 ('aliphatic cysts'; 25–28). 1. *Peridinium leonis* sensu Wall & Dale 1968 (Wadden Sea). 2. *Peridinium ponticum* (Thau Lagoon, Gulf of Lyon). 3. *Polykrikos kofoidii* sensu Matsuoka et al. 2009 (Olhão Port). 4. *Polykrikos kofoidii* sensu Matsuoka et al. 2009 (Ōmura Bay, East China Sea). 5-7 *Polykrikos kofoidii* sensu Matsuoka et al. 2009 (Wadden Sea). 8-9. *Polykrikos quadratus* (Lancaster Sound, Bylot Island). 10–11. *Polykrikos schwartzii* Matsuoka et al. 2009 (Isla San José). 12. *Polykrikos schwartzii* Matsuoka et al. 2009 (Qinhuangdao, Bohai Sea). 13. *Qia lebouriae* (Qinhuangdao, Bohai Sea). 14. *Quinquecuspis concreta* (Aveiro, Rua da Forta da Barra). 15–16. *Selenopemphix nephroides* (Portimão Port). 17. *Selenopemphix nephroides* (Qinhuangdao, Bohai Sea). 18. *Selenopemphix quanta* (Isla San José). 19–21. *Trinovantedinium pallidifulvum* (Qinhuangdao, Bohai Sea). 22. *Votadinium calvum* (Ōmura Bay, East China Sea). 23. *Trinovantedinium applanatum* (Olhão Port). 24. *Trinovantedinium applanatum* (Wadden Sea). 25–26. *Fusiperidinium wisconsinense* (Plastic Lake). 27–28. *Peridinium limbatum* (Plastic Lake). Scale bar = 20 µm. More info on samples and analyzed specimens can be found in Tables S1 and S3.

1248 Supplementary tables

1249

1250 Table S1. Overview and additional information of all surface sediment and rock samples used
1251 in this study.

1252

1253 Table S2. Complete ATR micro-FTIR dataset used and presented in this study (Figures 1–3).
1254 This table is in a format directly loadable into the Quasar software package (see materials and
1255 methods section).

1256

1257 Table S3. Metadata, counts and spectrochemical group assignments of all specimens and
1258 standards analyzed via ATR micro-FTIR spectroscopy in this study.

1259

1260 Table S4. The synchrotron transmission micro-FTIR dataset corresponding to the specimen
1261 presented in Figure 4a–b. This table is in a format directly loadable into the Quasar software
1262 package (see materials and methods section).

1263

1264 Table S5. The O-PTIR dataset corresponding to the specimens presented Figure 4c. This table
1265 is in a format directly loadable into the Quasar software package (see materials and methods
1266 section).

1267

1268 Supplementary videos

1269

1270 Video S1. Bleaching of a cyst of *Gymnodinium catenatum* under UV-A (385–330 nm)
1271 exposure. Captured at 1000 × using 1 $\text{frame} \cdot \text{s}^{-1}$. Playback speed is 8x (8 $\text{frames} \cdot \text{s}^{-1}$).

1272

1273 Video S2. Bleaching of a cyst of *Pentapharsodinium dalei* under UV-A (385–330 nm)

1274 exposure. Captured at 1000 × using 1 frame · s^{-1}. Playback speed is 8x (8 frames · s^{-1}).

1275

1276 Video S3. Bleaching of a cyst of *Archaeperidinium minutum* under UV-A (385–330 nm)

1277 exposure. Captured at 1000 × using 1 frame · s^{-1}. Playback speed is 8x (8 frames · s^{-1}).

1278

1279 Video S4. Bleaching of a cyst of *Dubridinium* sp. under UV-A (385–330 nm) exposure.

1280 Captured at 1000 × using 1 frame · s^{-1}. Playback speed is 8x (8 frames · s^{-1}).

Figure 1

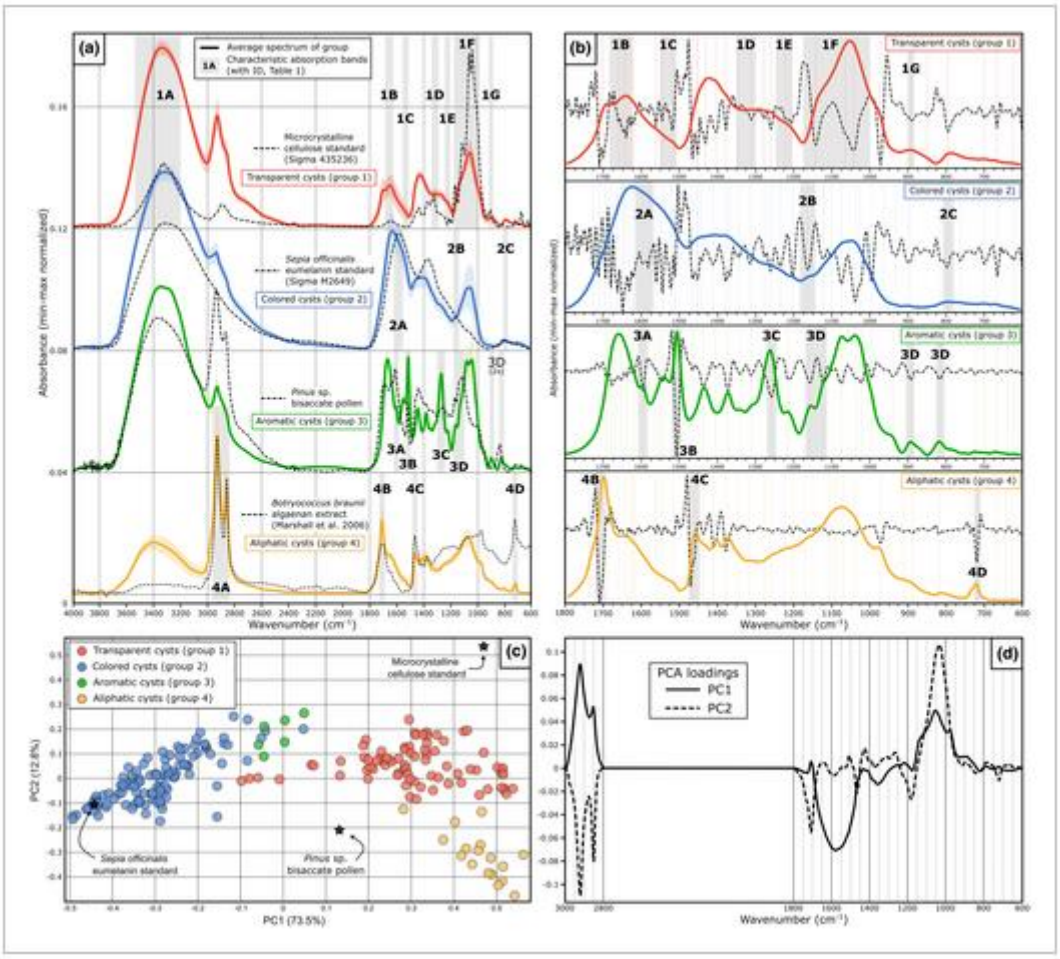
(a)
Average spectrum of group
Characteristic absorption bands (with ID, Table 1)
Microcrystalline cellulose standard (Sigma 435236)
Transparent cysts (group 1)
Sepia officinalis eumelanin standard (Sigma M2649)
Colored cysts (group 2)
Pinus sp. bisaccate pollen
Aromatic cysts (group 3)
Botryococcus braunii algaenan extract (Marshall et al. 2006)
Aliphatic cysts (group 4)
Absorbance (min-max normalized)
Wavenumber (cm⁻¹)
(b)
Transparent cysts (group 1)
Colored cysts (group 2)
Aromatic cysts (group 3)
Aliphatic cysts (group 4)
(c)
Transparent cysts (group 1)
Colored cysts (group 2)
Aromatic cysts (group 3)
Aliphatic cysts (group 4)
Microcrystalline cellulose standard
Sepia officinalis eumelanin standard
Pinus sp. bisaccate pollen
PC2 (12.8%)
PC1 (73.5%)
(d)
PCA loadings
PC1
PC2
Wavenumber (cm⁻¹)

Figure 2

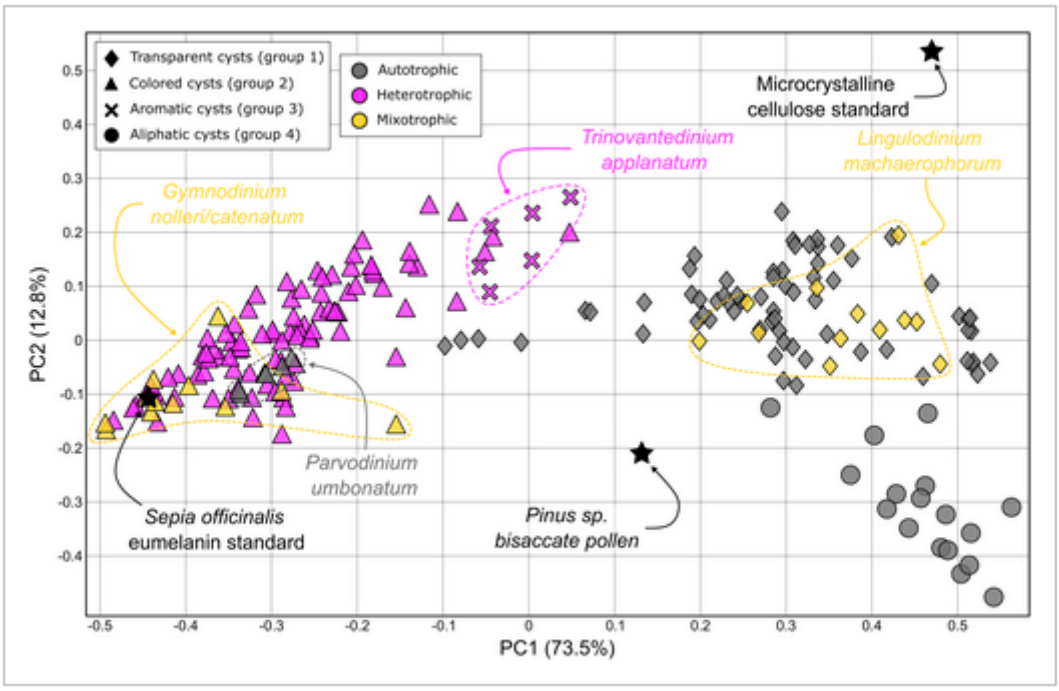
Transparent cysts (group 1)
Colored cysts (group 2)
Aromatic cysts (group 3)
Aliphatic cysts (group 4)
Autotrophic
Heterotrophic
Mixotrophic
Microcrystalline cellulose standard
Trinovantedinium applanatum
Lingulodinium machaerophorum
Gymnodinium nolleri/catenatum
Parvodinium umbonatum
Sepia officinalis eumelanin standard
Pinus sp. bisaccate pollen
PC2 (12.8%)
PC1 (73.5%)
0.5
0.4
0.3
0.2
0.1
0
-0.1
-0.2
-0.3
-0.4
-0.5
-0.4
-0.3
-0.2
-0.1
0
0.1
0.2
0.3
0.4
0.5

Figure 3

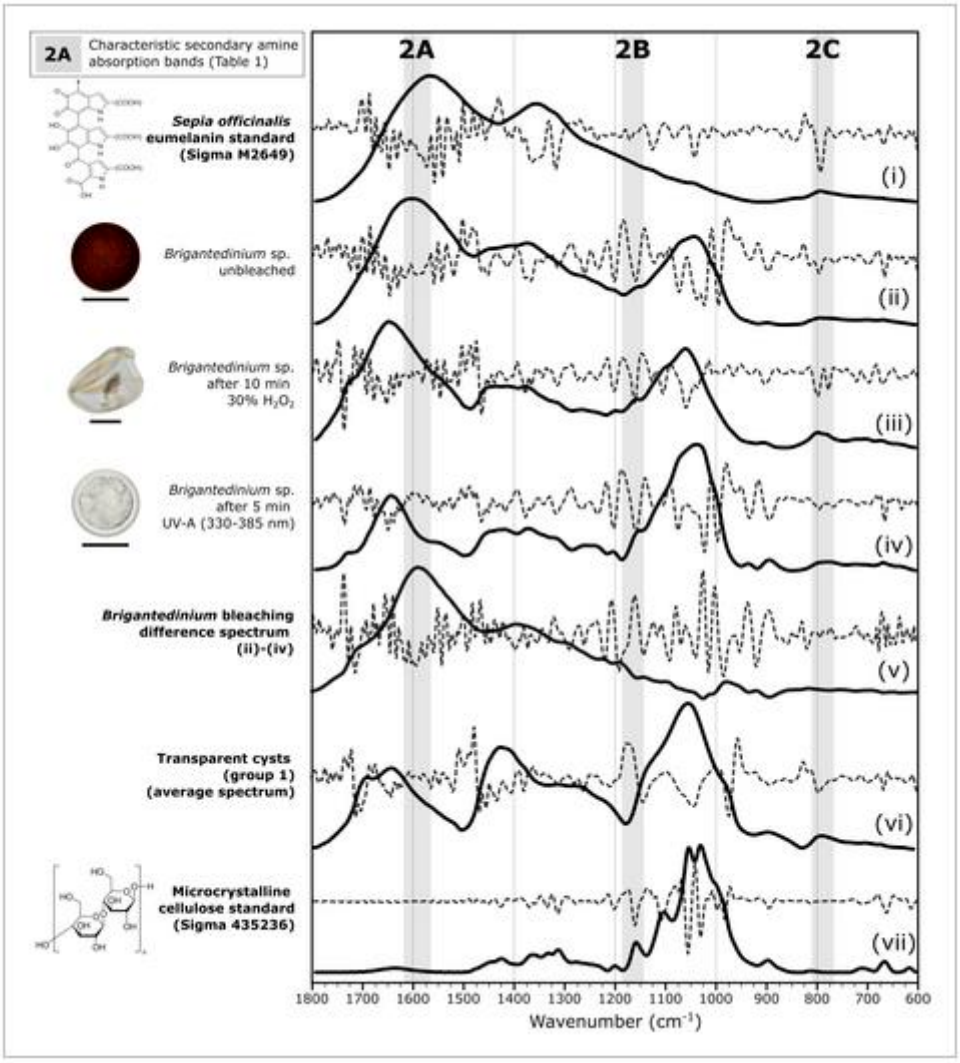
2A
Characteristic secondary amine absorption bands (Table 1)
Sepia officinalis eumelanin standard (Sigma M2649)
Brigantedinium sp. unbleached
Brigantedinium sp. after 10 min 30% H2O2
Brigantedinium sp. after 5 min UV-A (330-385 nm)
Brigantedinium bleaching difference spectrum (ii)-(iv)
Transparent cysts (group 1) (average spectrum)
Microcrystalline cellulose standard (Sigma 435236)
2A
2B
2C
(i)
(ii)
(iii)
(iv)
(v)
(vi)
(vii)
1800 1700 1600 1500 1400 1300 1200 1100 1000 900 800 700 600
Wavenumber (cm-1)

Figure 4

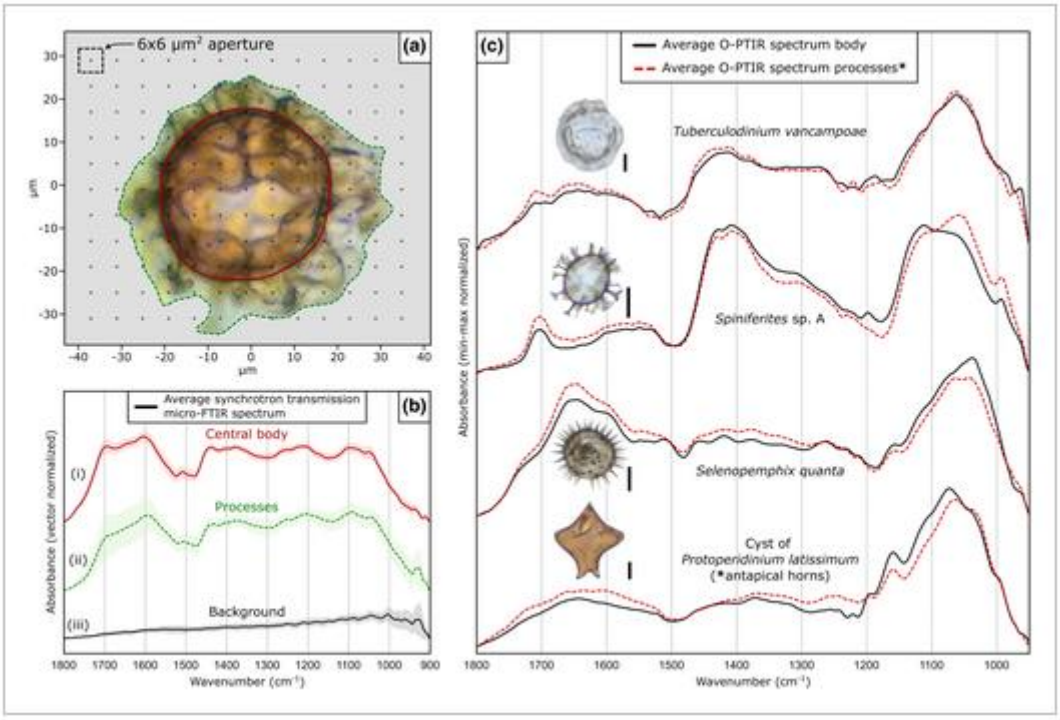
6x6 µm² aperture
(a)
µm
(b)
Average synchrotron transmission micro-FTIR spectrum
Central body
Processes
Background
(i)
(ii)
(iii)
Absorbance (vector normalized)
Wavenumber (cm⁻¹)
(c)
Average O-PTIR spectrum body
Average O-PTIR spectrum processes*
Tuberculodinium vancampoae
Spiniferites sp. A
Selenopemphix quanta
Cyst of Protoperidinium latissimum (*antapical horns)
Absorbance (min-max normalized)
Wavenumber (cm⁻¹)

TABLE 1 Overview of group frequencies identified from the ATR micro-FTIR spectra of dinocysts from modern surface sediments, with an indication of characteristic absorption bands for each erected spectrochemical group (Figure 1a,b).

Group frequency	Functional group	Transparent cysts (group 1)	Colored cysts (group 2)	Aromatic cysts (group 3)	Aliphatic cysts (group 4)	Reference	ID (Figure 1a,b)
3550–3200	Hydroxy group → H-bonded O–H stretching	S	S	S	M	Coates (2000)	1A
2985–2975	Methyl ($-CH_3$) → C–H asymmetrical/symmetrical stretching	A	A	A	W	Coates (2000)	
2955–2915 2870–2845	Methylene ($>CH_2$) → C–H asymmetrical/symmetrical stretching	S	M	M	VS	Coates (2000)	4A
1720–1695	Carbonyl → Ketone and/or carboxylic acid C=O stretching	M	W	W	S	Coates (2000)	4B
1687–1626	Amide I → C=O stretching	W	S	S	M	Bogus et al. (2014)	1B
1620–1570	Secondary amine (>N–H) 'eumelanin' → N–H stretching	A	M	A	A	Coates (2000)	2A
1610–1585	C=C–C Aromatic ring stretching	A	A	M	A	Coates (2000)	3A
1550–1535	Amide II → N – H bending	W	S	M	W	Meyvisch et al. (2022)	1C
1535–1515	Amide II → C – N stretching	W	S	A	W	Meyvisch et al. (2022)	1C
1520–1495	C = C – C Aromatic ring stretching	A	A	S	A	Coates (2000)	3B
1475–1445	Methylene ($> CH_2$) → C – H bending	M	M	M	S	Coates (2000)	4C
1445–1350	CH_2 wagging	M	M	M	M	Colthup et al. (1990)	
1350–1300	Hydroxy group → O – H in-plane bending	W	W	W	W	Coates (2000)	1D
1280–1250	C – H Aromatic ring bending	A	A	S	A	Coates (2000)	3C
1245–1205	Amide III → N – H bending and C – H stretching	W	W	W	W	Bogus et al. (2014)	1E
1185–1145	Secondary amine (> N – H) 'eumelanin' → C – N stretching	A	W	A	A	Coates (2000)	2B
1175–1000	Polysaccharide (C – O – C, C – O and C – OR) ring stretching	M	M	S	M	Bogus et al. (2014)	1F
1170–1150 1135–1115	C – H Aromatic ring in- and out-of-plane bending	A	A	W	A	Coates (2000)	3D
905–885 825–805	(several bands)						

TABLE 1 (Continued)

Group frequency	Functional group	Transparent cysts (group 1)	Colored cysts (group 2)	Aromatic cysts (group 3)	Aliphatic cysts (group 4)	Reference	ID (Figure 1a,b)
1155–1130	Asymmetric ether C – O – C stretching	M	A	A	A	Coates (2000)	
1005–985	Monosubstituted alkene C = C bending	W	A	A	M	Meyvisch et al. (2022)	
905–885	C – H wagging of β-glycosidic bond	W	W	W	W	Bogus et al. (2014)	1G
810–780	Secondary amine (> N – H) 'eumelanin' → N – H wagging and/or twisting	A	W	A	A	Colthup et al. (1990)	2C
725–710	Methylene (> CH_2) → $(CH_2)_n$-rocking ($n \geq 3$)	A	A	A	W	Coates (2000)	4D
675–655	C – OH out-of-plane bending	W	W	W	W	Meyvisch et al. (2022)	

Note: Absorption band identifications are based on Bogus et al. (2014), Coates (2000), Colthup et al. (1990), and Meyvisch et al. (2022).

Abbrevations: VS = very strong, S = strong, M = medium, W = weak, A = absent.